Check for updates

The role of Ce addition in catalytic activity enhancement of TiO_2-supported Ni for CO_2 methanation reaction†

Ammarika Makdee,[a] Kingkaew Chayakul Chanapattharapol, [ID] *[a] Pinit Kidkhunthod,[b] Yingyot Poo-arporn[b] and Teruhisa Ohno [ID] [c]

In this work, various amounts of Ce were added to TiO_2 to form a mixed oxide support; $Ce_xTi_{1-x}O_2$ ($x = 0$, 0.003, 0.05, 0.10 and 0.15) and then those synthesized supports were impregnated by 10 wt% Ni to produce a catalysts. The 10 wt% Ni–$Ce_xTi_{1-x}O_2$ ($x = 0$, 0.003, 0.05, 0.10 and 0.15) catalysts were tested for CO_2 methanation reaction by using a fixed-bed reactor in the temperature range of 100–500 °C. The sample was pretreated at 450 °C under H_2 and then a mixed feed gas of CO_2 and H_2 was switched into the reactor to start the reaction. The results showed that 10 wt% Ni–$Ce_{0.003}Ti_{0.997}O_2$ catalyst (the lowest Ce content) exhibited the highest CO_2 conversion and CH_4 yield. Moreover, 10 wt% Ni–$Ce_{0.003}Ti_{0.997}O_2$ showed highly stable during the stability test (50 h.). The results indicated that upon addition of small amount of Ce into TiO_2-supported Ni, the surface, structural, electrical and redox properties of the catalyst were improved to the extent that these properties can promote the catalytic activities for CO_2 methanation. The Ce addition can improve the CO_2 methanation catalytic activity by several ways. First, higher dispersion of Ni on catalysts surface upon addition of Ce was observed which resulted in higher adsorption rate of H_2 on this metal active site. Second, formation of a larger amounts of oxygen vacancies as well as basicity improvement upon addition of Ce were occurred which can increase the CO_2 adsorption on catalyst surface. Third, incorporation of Ce resulted in improving of a starting reduction temperature of Ni^{2+} to Ni^0 for TiO_2-supported Ni catalyst which can indicate that the reducibility of Ce-doped TiO_2-supported Ni catalyst was enhanced and then alter its catalytic activity. However, increasing of Ce content led to lowering of CO_2 methanation activities which resulted from increasing of basicity by Ce addition. The excess amounts of adsorbed CO_2 would lead to competitive adsorption to H_2 and then lead to a decrease of catalytic activity. Therefore, an appropriate amount of H_2 and CO_2 adsorption ability on catalyst surface was a prominent factor to dominate the catalytic activity.

1. Introduction

Carbon dioxide (CO_2) is one of the greenhouse gases which is the most abundant in the atmosphere. It is the biggest contributor to the earth's temperature increases and climate change which are currently a main global problem. The concentration of CO_2 in the atmosphere can be reduced by two methods (i) CO_2 capture and storage (CCS) and (ii) CO_2 conversion and utilization (CCU). However, while CO_2 capture

and storage is an important way to rapidly decrease CO_2 levels in the atmosphere, the disadvantage of this method is the possible leakage of captured CO_2.[1] Therefore, CO_2 conversion and utilization is a preferred method. This method not only reduces CO_2 concentration but also generates useful products and fuels which respond to high energy demands. CO_2 hydrogenation to form CH_4 by using H_2 as a reductant is one of the most common reactions which is used to decrease CO_2 concentration and produce CH_4. This reaction can be called CO_2 methanation or Sabatier reaction according to eqn (1):

$$CO_2 + 4H_2 \rightarrow CH_4 + 2H_2O, \Delta H_{298\ K} = -165.12 \text{ kJ mol}^{-1} \quad (1)$$

One interesting benefit of CO_2 methanation reaction is that the product, CH_4, can be directly injected into natural gas pipelines, can be used as a starting material for the production of other chemicals and can be utilized as an energy carrier due to the transportation of H_2 is limited. In addition, CO_2 methanation can be performed under atmospheric pressure and low

[a]Materials Chemistry Research Center, Department of Chemistry, Center of Excellence for Innovation in Chemistry, Faculty of Science, Khon Kaen University, Khon Kaen, 40002, Thailand. E-mail: kingkaew@kku.ac.th; Fax: +66 432 02373; Tel: +66 430 09700 ext. 12371

[b]Synchrotron Light Research Institute (Public Organization), Nakhon Ratchasima 30000, Thailand

[c]Department of Applied Chemistry, Faculty of Engineering, Kyushu Institute of Technology, 1-1 Sensuicho, Tobata, Kitakyushu 804-8550, Japan

† Electronic supplementary information (ESI) available. See DOI: 10.1039/d0ra04934d

temperature due to its exothermic characteristics and it is also considerably faster than other reactions such as hydrogenation of CO_2 to alcohol.[2] However, this reaction needs eight electrons to convert CO_2 to CH_4 which is a significant kinetic barrier.[3] Moreover, some side-reactions can occur at high temperature, such as reversed water gas shift ($CO_2 + H_2 \rightarrow CO + H_2O$) which can lead to lower CH_4 selectivity.[4] Therefore, catalysts must be employed in order to achieve a high reaction rate and high CH_4 selectivity.[5–8] In recent years, many research groups have been interested in CO_2 methanation by using heterogeneous catalysts. It has been reported that supports and active species on catalyst surfaces affected the CO_2 methanation catalytic activities of catalysts. For the active species, noble metals such as Ru and Rh provided the highest catalytic activities and CH_4 selectivities.[2,9] However, they are very expensive. Therefore, other metals with a lower price have been employed instead. Ni metal was widely used as an active species due to its inexpensive and high catalytic activity.[9–16] The Ni metal is the most favorable active species for H_2 dissociation to form atomic H which facilitates the CH_4 formation and results in the enhancement of CO_2 conversion and CH_4 selectivity.[17,18] The catalyst support also displays an important role in the catalytic activity of the catalyst. Recently, many metal oxides have been widely used as catalyst supports such as Al_2O_3, SiO_2, ZrO_2, TiO_2, and CeO_2.[19–21] Among these supports, reducible supports (TiO_2, CeO_2, and ZrO_2) were widely selected because of their excellent redox properties. Due to the CO_2 methanation mechanism involved in the redox process, the reaction rate can be enhanced by facilitating this process. To increase the redox properties of metal oxide supports, some metals have been used to incorporate into the metal oxide lattice. These metals are called promoters. Several works have reported on the use of rare earth metals (La, Ce, Sm) as promoters in CO_2 methanation reaction due to their functionality to catalyze the reaction rate by for example, modifying the surface properties, redox properties, electrical properties and surface basicity.[22–29] Cerium oxide was usually used as a promoter due to its superior properties on improving the surface basicity and oxygen vacancies formation through valence change between Ce^{3+} and Ce^{4+}.[30,31] Bian et al.[30] reported the effect of CeO_2 addition as a promoter on Ni/Al_2O_3 catalysts. They found that the surface basicity and Ni dispersion on catalyst surfaces were improved upon the addition of CeO_2 which resulted in high CO_2 methanation activity in low-temperature ranges. Tada et al.[31] reported that CeO_2 plays an important role in promoting CO_2 methanation and enhancing CH_4 formation. CeO_2 can improve the surface basicity in which CO_2 can be easily adsorbed and reduced due to oxygen vacancies formation by addition of CeO_2 into Ru/Al_2O_3. Moreover, they found that the specific surface area of the catalyst was enhanced upon the addition of CeO_2.

In this work, we report on the catalytic activity of TiO_2-supported Ni catalysts for CO_2 methanation. Since, the reported on using TiO_2 as a catalyst support for CO_2 methanation is now still being developed, therefore, it is of interested and challenged to improve the TiO_2 catalysts performance which can provide a better catalytic activity and can also produce the desired products. Ce was used as a promoter to modify the TiO_2-supported Ni properties by incorporating it into TiO_2 crystal structure in the form of $Ce_xTi_{1-x}O_2$ mixed oxides. All of these catalysts were tested for catalytic activity for CO_2 methanation and characterized by standard characterization methods such as X-ray diffraction (XRD), N_2 adsorption–desorption, H_2 adsorption, CO_2 adsorption, transmission electron microscopy (TEM), scanning electron microscopy (SEM), inductively coupled plasma-optical emission spectroscopy (ICP-OES), X-ray photoelectron spectroscopy (XPS) and X-ray absorption spectroscopy (XAS). All of these results were used to describe the role of Ce addition on enhancing the CO_2 methanation reaction of TiO_2-supported Ni.

2. Experimental

2.1 Materials

All chemicals in this experiment were analytical grade without further purification. Titanium(IV) isopropoxide (98+%) and cerium(III) nitrate hexahydrate (99.5%) were purchased from Acros Organics. Ethanol absolute anhydrous (99.9%) and nickel(II) nitrate hexahydrate (99%) were purchased from Carlo Erba. Nitric acid (65%) was provided by Acl Labscan. Deionized water was used for all preparations.

2.2 Preparation of TiO_2, $Ce_xTi_{1-x}O_2$, TiO_2-supported Ni and $Ce_xTi_{1-x}O_2$-support Ni

TiO_2 support was prepared by sol–gel method with titanium isopropoxide as a starting precursor. Titanium isopropoxide was first dissolved in ethanol, then DI water and HNO_3 were added dropwise to Ti precursor solution and continuously stirred for 3 h. The mixture was dried at 100 °C for 24 h and calcined at 400 °C for 3 h. $Ce_xTi_{1-x}O_2$ mixed oxide supports were also prepared by the same method as TiO_2 support with Ce/Ti molar ratio of 1/200, 1/20, 1/10 and 1/5. The preparation procedure was the same as described above in which the aqueous solution of $Ce(NO_3)_3 \cdot 6H_2O$ was co-added together with DI water and HNO_3.

10 wt% Ni doped TiO_2 and $Ce_xTi_{1-x}O_2$-supported were prepared by incipient wetness impregnation method. $Ni(NO_3)_2 \cdot 6H_2O$ was used as a Ni precursor. An appropriate amount of precursor salt was dissolved in DI water. After that, the precursor solution was added to the prepared supports and then dried at 100 °C for 24 h and calcined at 400 °C for 3 h.

2.3 Catalysts characterization

X-ray diffraction (XRD) patterns of all catalysts were obtained from PANalytical Empyrean with Cu Kα radiation wavelength of 1.5406 Å. The obtained patterns were scanned in the 2θ range of 10° to 80°. The crystalline size (D) was calculated from Scherrer's equation as:

$$D = \frac{0.9\lambda}{\beta \cos \theta} \quad (2)$$

where λ is the X-ray wavelength, β is the broadening (in radians) at a half intensity of the TiO_2 (101) plane and θ is the diffraction

angle. Lattice parameters (a, b, c) were calculated from Bragg's equation by using (101), (004) and (200) planes of TiO_2.

The specific surface area of the prepared catalysts was calculated from N_2 adsorption–desorption isotherm at 77 K by Quantachrome NOVA 4200e instrument. Before the adsorption experiment, the catalysts were degassed at 100 °C for 1 h to clean the catalyst surface. The specific surface area was calculated by using the multipoint-BET method.

The morphology of the prepared catalysts was studied by transmission electron microscope (TEM) FEI/TECNAI G2 20. The catalysts were prepared by dispersing a catalyst powder in acetone with sonication and dropped on the copper grid before the scanning process.

Nickel dispersion mapping on catalysts surface was investigated by using a LEO 1450VP SEM-EDS instrument. Before scanning, the catalyst was dispersed on a carbon tape which was attached on a specimen stub and coated with gold to reduce the electron charge.

The metals content in the prepared catalysts can be determined by using inductively coupled plasma-optical emission spectroscopy (ICP-OES). Before measuring the metal content, the catalysts (0.020–0.025 g) were digested by using a mixture of 6 mL concentrated H_2SO_4 and 2 mL 30% H_2O_2 at high temperature. The standards and samples solution in the range of 0–10 ppm were analyzed by optima 100DVICP-OES (PerkinElmer). The detection wavelengths for Ce and Ni were 413.764 and 231.604 nm, respectively.

X-ray photoelectron spectroscopy (XPS) was used to investigate the surface components of the catalysts. Ti 2p XPS spectra of the catalysts were obtained by using a KRATOS AXIS-NOVA (Shimadzu Corporation) instrument with a monochromatic Al K_α as an X-ray source. The binding energy shift caused by relative surface charging was corrected by using the C 1s level (284.8 eV) as an internal standard. The XPS peaks were assumed to be Gaussian peaks and were resolved into each component by using XPSPEAK41 software.

2.4 CO_2 and H_2 adsorption experiments

In order to investigate the adsorption ability of both reactants in CO_2 methanation reaction, the CO_2 and H_2 adsorption experiments were conducted at room temperature and under ambient pressure. For the CO_2 adsorption experiment, the catalyst (0.13–0.14 g) was dispersed on a glass dish which was placed in a Tedlar bag. After that, 150 mL of mixed gas was injected into the Tedlar bag. The mixed gas consisted of 500 ppm CO_2 and air (79% N_2 and 21% O_2). The concentration of CO_2 was monitored every 30 min for 4 h by withdrawing the gas from the bag and detected by gas chromatograph (INFICON 3000 Micro GC) with a PLOT U column and TCD detector. The amount of adsorbed CO_2 was calculated by subtracting the remaining CO_2 concentration at interval times from the initial CO_2 concentration. Finally, the relationship between adsorbed CO_2 amounts as a function of time was constructed.

The H_2 adsorption experiment was conducted in a similar manner as CO_2 adsorption experiment. The same amount of catalyst was spread on a glass dish and was placed in a Tedlar

bag. The 150 mL of mixed gas (500 ppm H_2 and air; 79% N_2 and 21% O_2) was injected into the bag and the adsorption experiment was left at room temperature for 4 h. After that, the remaining H_2 amount was detected by gas chromatograph (Agilent Technologies 490 Micro GC) with a MS-5A column and TCD detector. The H_2 uptake on the catalyst was calculated by using the same equation as the CO_2 adsorption experiment. The data reported in this manuscript is an average of three reproducible experiments.

2.5 X-ray absorption spectroscopy (XAS)

2.5.1 X-ray absorption near edge structure (XANES). The XAS experiment together with analysis the data in XANES region was carried out into two parts: XANES experiment for *ex situ* and *in situ* investigations. For the *ex situ* experiment, three samples (freshly prepared, pretreated and used catalysts) were used to study the oxidation states of all metals in the catalysts. In addition, the *in situ* experiment was used to monitor the changing of electronic states of Ni, Ti and Ce during CO_2 methanation reaction.

The XANES experiments were carried out on Beamline 2.2 (time-resolved X-ray absorption spectroscopy) at the Synchrotron Light Research Institute (SLRI), Nakhon Ratchasima, Thailand. The bent crystal was used as an energy dispersive monochromator. A Si (111) crystal was used as a monochromator with an energy range of 2.4–10 keV. The linear image sensor was used as a detector. For the *ex situ* experiment, the sample was first mixed with boron nitride (BN) to obtain a homogeneous powder and pressed into a pellet and attached on the sample frame. The XANES spectra were recorded in the K (for Ni and Ti) and L_3 (for Ce) edges energy in transmission mode. The ionization chamber was used as a detector and was placed in front of and behind the sample. For the *in situ* experiment, the sample was mixed with boron nitride, pressed into a pellet and then placed in an *in situ* cell. The sample was first pretreated by heating the sample cell from room temperature to 450 °C (ramp rate of 5 °C min^{-1}) under H_2 flowing at 24 mL min^{-1}. The spectra were collected every 10 °C increment as the temperature increased. Next, the temperature was kept at 450 °C for 90 min, in order to reduce Ni ion species to metallic Ni, and the spectra were collected every 10 min. After the pretreatment, the temperature was reduced to 100 °C and the mixed feed gas composition of H_2 (24 mL min^{-1}) and CO_2 (6 mL min^{-1}) with the ratio of 4 : 1 was switched into the *in situ* cell to start the CO_2 methanation reaction. The reaction temperature was kept at 100 °C for 20 min and the spectra were collected every 10 min at this point. After that, the reaction temperature was increased to 150 °C (ramp rate of 5 °C min^{-1}) and the spectra were collected at every 10 °C increment. When the reaction temperature reached 150 °C, the spectra were collected every 10 min for 20 min. Then, the reaction temperature was increased by 50 °C and the spectra were recorded during the increase and then holding the reaction temperature as described above. The reaction temperature range was 100–500 °C. The XANES spectra were obtained by subtracting I_1 by I_0

with the preprocessing software before being exported to Athena software.

2.5.2 Extended X-ray absorption fine structure (EXAFS). The XAS experiment with the data analysis in the EXAFS region was used to investigate the local environment changes during a CO_2 methanation reaction. In this experiment, the local environment change of Ni was probed as this species is believed to be an active component which plays an important role in enhancing the reaction. The *in situ* EXAFS experiment was investigated under the CO_2 methanation conditions which were similar to the *in situ* XANES experiment. Firstly, a pretreatment was carried out by ramping the sample from room temperature to 450 °C at the rate of 5 °C min⁻¹ under H_2 flow (20 mL min⁻¹). After the temperature reached 450 °C, the temperature was held at this point for 90 min with the same flow rate of H_2 and data was collected. After finishing the pretreatment process, the temperature was decreased to 100 °C under H_2 flow. Secondly, the reaction was started at 100 °C. The feed gas was switched to the mixture of CO_2 (5 mL min⁻¹) and H_2 (20 mL min⁻¹). The temperature was kept constant at 100 °C for 25 min and data was recorded. After that, the temperature was increased with the rate of 5 °C min⁻¹ to 150 °C and was kept constant at this point for 25 min and the data was recorded. In the next step, the reaction temperature was increased by 50 °C for each step until it reached 550 °C with the same ramp rate and data collection procedure. The Ni K edge EXAFS spectra of the catalyst during CO_2 methanation condition can be obtained on a SUT-NANOTEC-SLRI beamline 5.2 at the Synchrotron Light Research Institute (SLRI), Nakhon Ratchasima, Thailand.[32,33] The measurement was carried out in transmission mode. Synchrotron radiation was tuned by a double crystal monochromator (DCM) equipped with Ge (220) crystal. The monochromatic flux was 10^8–10^{10} photons per s at 100 mA. Ionization chambers were used as a detector which was installed in front of and behind the sample to detect the incident (I_0) and transmitted (I_1) beam. The collected data were analyzed by Athena and Artemis software.

2.6 CO_2 methanation catalytic activity test

The catalytic activity of the prepared catalyst was tested for CO_2 methanation reaction. The CO_2 methanation reaction was studied in a flow reactor with the temperature in the range of 100–500 °C. The 50 mg of catalyst was sandwiched between two layers of quartz wool in the Pyrex tube. This Pyrex tube was placed inside the controllable temperature furnace. The K-type thermocouple was inserted at the top of the catalyst bed to monitor the reaction temperature. The feed gases flow rate was controlled by mass flow controllers. Before starting CO_2 methanation, the catalyst was pretreated at 450 °C under H_2 atmosphere with a flow rate of 50 mL min⁻¹ for 1.5 h. The CO_2 methanation was started by using mixed feed gas of CO_2, H_2 and He with a flow rate of 6, 24 and 10 mL min⁻¹, respectively. The mixed feed gas was passed through the catalyst in the Pyrex tube and then the reactants and products were analyzed by on-line Agilent Technologies 6890N gas chromatograph with HEYSEP D packed column and TCD was used as a detector. The

percentages of CO_2 conversion, products yield, and selectivity were calculated by using the following equations;

$$\% \ CO_2 \text{ conversion} = \left(1 - \frac{[CO_2]_{out}}{[CO_2]_{out} + [CH_4]_{out} + [CO]_{out}} \right) \times 100 \quad (3)$$

$$\% \ CH_4 \text{ or CO yield} = \left(\frac{[CH_4]_{out} \text{ or } [CO]_{out}}{[CO_2]_{out} + [CH_4]_{out} + [CO]_{out}} \right) \times 100 \quad (4)$$

$$\% \ CH_4 \text{ or CO selectivity} = \left(\frac{CH_4 \text{ or CO yield}}{CO_2 \text{ conversion}} \right) \times 100 \quad (5)$$

where $[CO_2]_{out}$, $[CH_4]_{out}$ and $[CO]_{out}$ are outlet concentration of CO_2, CH_4, and CO, respectively.

In order to exclude the heat and mass transfer under the kinetic reaction rate condition (reaction temperature range 230–280 °C), the separated experiments were conducted. The weight of catalyst (W) and total feed volume (F_{total}) were varied while the GHSV was kept constant.[34] Two set of the same ratio between W/F_{total}; 0.05 g/40 mL min⁻¹ and 0.1 g/80 mL min⁻¹, were tested for CO_2 methanation condition. The results showed that the CO_2 conversion of 10 wt% Ni–Ce$_{0.003}$Ti$_{0.997}$O$_2$ sample were similar for two sets (5.8% and 6.2%, respectively) at 250 °C.

3. Results and discussion

3.1 Standard characterization

3.1.1 XRD, N_2 adsorption–desorption, TEM and SEM. The XRD patterns of TiO_2 and 10 wt% Ni–Ce$_x$Ti$_{1-x}$O$_2$ ($x = 0$, 0.003, 0.05, 0.10 and 0.15) are displayed in Fig. 1. All synthesized samples exhibited diffraction peaks at 25.2°, 37.8°, 48.1°, 53.9°, 55.2°, 62.9°, 68.9°, 70.2° and 75.2° which corresponded to the (101), (004), (200), (105), (211), (204), (116), (220) and (215) crystallographic planes of anatase TiO_2 (JPCDS file number 21-1272), respectively.[35–38] The unit cell parameters of all catalysts
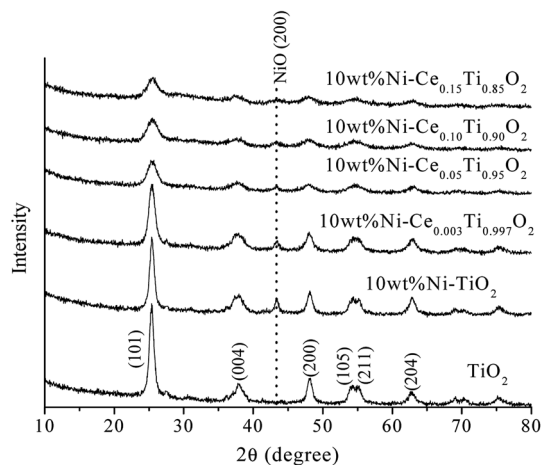

Fig. 1 XRD patterns of TiO_2 and 10 wt% NiCe$_x$Ti$_{1-x}$O$_2$ ($x = 0$, 0.003, 0.05, 0.10 and 0.15) catalysts.

Table 1 Crystalline size, unit cell parameters, surface area and metals content of the catalysts

| Catalyst | Crystalline size[a] (Å) | Lattice parameters[b] | | Cell volume (Å^3) | Surface area[c] ($m^2\,g^{-1}$) | Ni[d] (wt%) | Ce[d] (mol%) |
		$a = b$ (Å)	c (Å)				
TiO_2	103.9	3.786	9.503	136.2	138.02	—	—
10 wt% Ni–TiO_2	108.6	3.793	9.568	137.7	67.63	11.01	—
10 wt% Ni–$Ce_{0.003}Ti_{0.997}O_2$	76.8	3.802	9.581	138.5	82.16	10.78	0.24
10 wt% Ni–$Ce_{0.05}Ti_{0.95}O_2$	62.6	3.833	9.676	142.1	123.48	10.87	4.11
10 wt% Ni–$Ce_{0.10}Ti_{0.90}O_2$	54.2	3.834	9.795	143.9	136.87	11.44	9.40
10 wt% Ni–$Ce_{0.15}Ti_{0.85}O_2$	51.5	3.850	9.935	147.3	150.03	12.61	15.30

[a] Calculated from (101) plane of TiO_2 using Sherrer's equation. [b] Calculated from (101), (004), (200) planes of TiO_2 using Bragg's equation. [c] Calculated by using multipoint BET method. [d] Calculated from ICP-OES results.

were calculated by using (101), (004) and (200) crystallographic planes and were summarized in Table 1. The unit cell parameters of TiO_2 were in accordance with other works.[39,40] Addition of Ni and Ce led to structural changing of TiO_2 support. In the case of 10 wt% Ni–TiO_2, the additional diffraction peak at around 43.2° was observed which corresponded to (200) plane of cubic NiO (JPCDS file number 47-1049).[38,41] It can be seen that the calculated unit cell parameters were increased upon only impregnation of Ni onto TiO_2 which then led to an increase of unit cell volume. It is noteworthy that the amount of impregnated Ni onto the support was kept constant at around 10 wt%, but the NiO diffraction peaks were remarkably decreased upon the increase of Ce content. This may be due to the decreasing crystalline size of the sample, which can be observed by the lowering and broadening of XRD peaks, as illustrated in Table 1. The decrease in TiO_2 crystalline size may have resulted in small particle size of impregnated Ni on the catalyst surface which then led to a lowering of NiO diffraction peaks. Therefore, this can indicate that the addition of Ce into TiO_2 would lead to the inhibition of TiO_2 crystal growth.

In a comparison between different Ce loading catalysts, the characteristic peaks of cerium oxide were not observed, which indicated that Ce ions probably incorporated into TiO_2 lattice by replacing Ti sites or interstitial sites to form a solid solution.[42,43] These results could be confirmed by the expansion of the cell parameters with increased Ce content (Table 1). Additionally, the results of enlargement of TiO_2 upon the addition of Ni and Ce indicated the incorporation of both larger Ni (Ni^{2+} = 0.69 pm) and Ce (Ce^{3+} = 1.01 pm) into the TiO_2 (Ti^{4+} = 0.60 pm) lattice. It can be reported that the incorporation of added metal into the host lattice depended on the synthesis method. The sol–gel method usually produced the mixed oxide materials formed by replacing of host ions by added ions,[42,44–47] while the impregnation method also produced the incorporation of added metal.[48] To confirm the incorporation of added metals into TiO_2, X-ray absorption spectroscopy in the region of extended X-ray absorption fine structure was studied and is further discussed in the next section.

Fig. 2 exhibits N_2 adsorption–desorption isotherms of the prepared catalysts. The isotherm feature of TiO_2 was similar to type IV isotherm with a hysteresis loop which indicated the existence of the mesoporous structure.[37,49] When Ni and Ce

metals were added into TiO_2, the isotherm feature remained unchanged which indicated that the incorporation of Ni and Ce species into TiO_2 did not alter the textural properties of TiO_2. The calculated BET surface area of the prepared catalysts is presented in Table 1. The BET surface area of TiO_2 was 138.02 $m^2\,g^{-1}$ and decreased to 67.63 $m^2\,g^{-1}$ for 10 wt% Ni–TiO_2 which could be due to a partial blockage or collapse of small mesopores during the impregnation of Ni.[12] In contrast, for Ce added samples, the specific surface area was increased with increased Ce content, which was due to the lowering of crystalline size of TiO_2 crystal.

The Ni and Ce contents in 10 wt% Ni–$Ce_xTi_{1-x}O_2$ (x = 0, 0.003, 0.05, 0.10 and 0.15) catalysts can be determined by using inductively coupled plasma-optical emission spectroscopy (ICP-OES), and the results are summarized in Table 1. The Ni amount of all catalysts exhibited a similar value at around 10 wt%. The calculated Ce content was 0.24, 4.11, 9.40 and 15.30 mol% which corresponded to the value of x for 10 wt% Ni–$Ce_xTi_{1-x}O_2$ (x = 0.003, 0.05, 0.10 and 0.15). The morphologies of TiO_2 and 10 wt% Ni–$Ce_xTi_{1-x}O_2$ (x = 0, 0.003 and 0.10) catalysts were studied by using high-resolution TEM and the images are displayed in Fig. 3. All samples (for the left-hand side images)
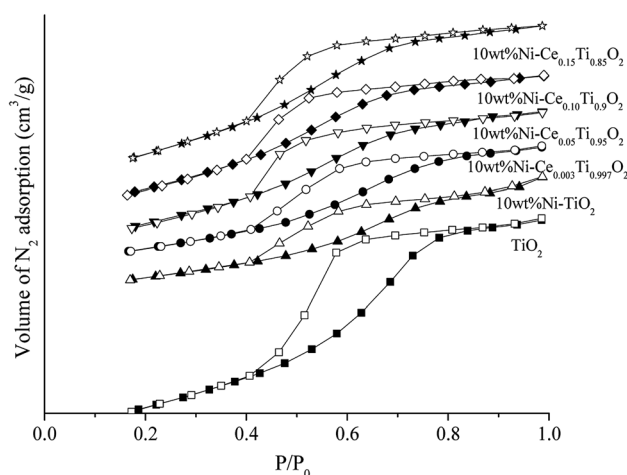

Fig. 2 N_2 adsorption–desorption isotherms of TiO_2 and 10 wt% Ni–$Ce_xTi_{1-x}O_2$ (x = 0, 0.003, 0.05, 0.10 and 0.15) catalysts. A solid symbol is adsorption branch and open symbol is desorption branch.
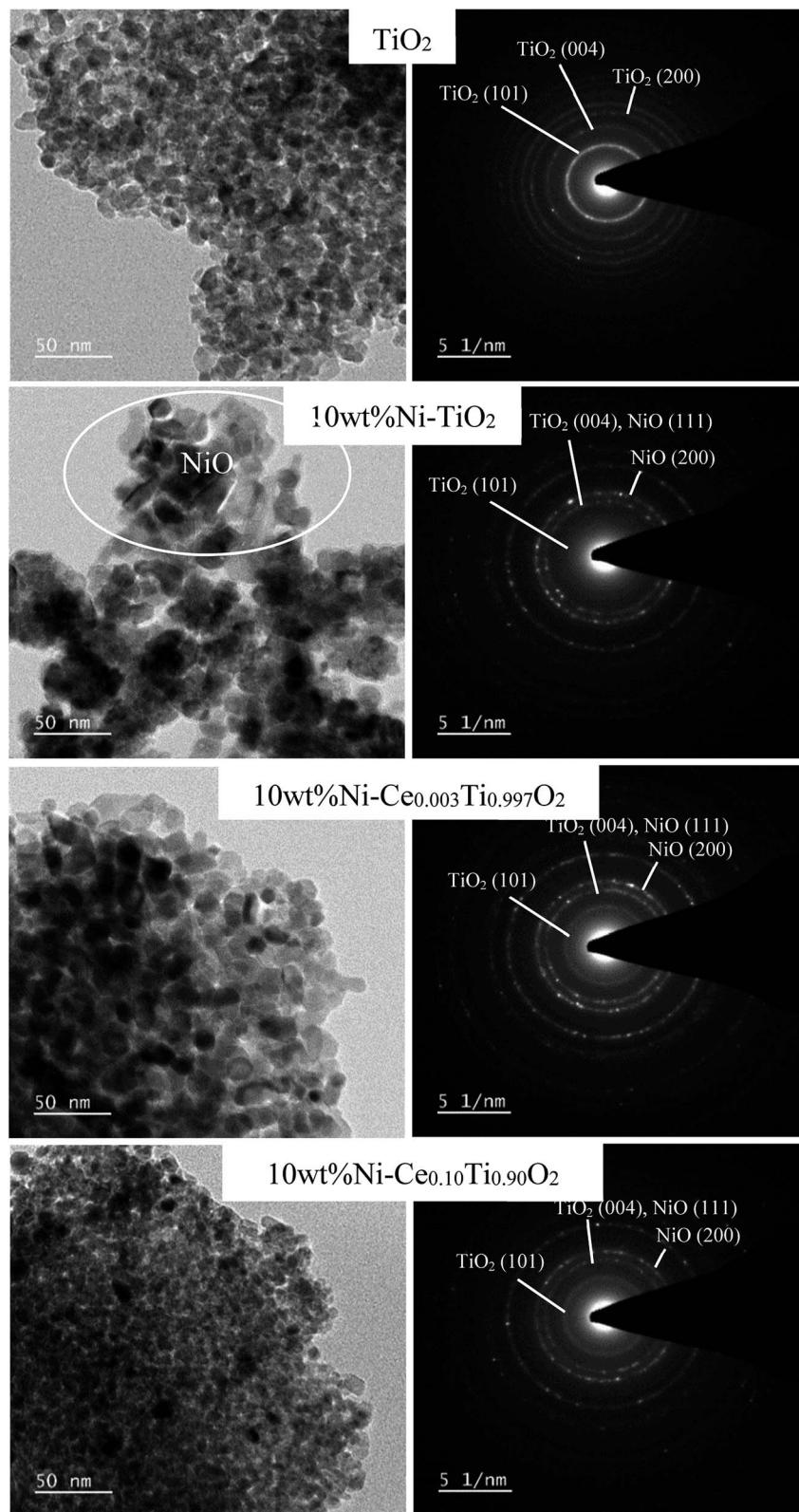
Fig. 3   TEM images and selected area of electron diffraction patterns of TiO_2 and 10 wt% $Ni-Ce_xTi_{1-x}O_2$ ($x = 0$, 0.003 and 0.10) catalysts.

exhibit a spherical structure, compared to nanoaggregates assembled from many small nanocrystals, which led to the formation of a mesoporous structure. Moreover, upon incorporating Ce, the nanocrystal sizes were decreased, which corresponded to the XRD results. The right-hand side of Fig. 3 shows the selected area electron diffraction (SEAD) patterns of

the corresponding samples. For TiO_2, several diffraction planes were indexed to anatase TiO_2 [(001), (004) and (200)], while for doped samples, the SEAD patterns exhibited several diffraction rings pattern which indicated a polycrystalline structure.[46] Fig. 4 displays SEM and mapping images of Ni on catalysts surface for TiO_2 and 10 wt% Ni–$Ce_xTi_{1-x}O_2$ (x = 0, 0.003 and 0.10). The loading amount of Ni was kept constant around 10 wt% for all samples, therefore, different Ni dispersion should be resulted from Ce addition. It is seen that 10 wt% Ni–$Ce_{0.003}Ti_{0.997}O_2$ exhibited the highest dispersion of Ni on catalyst surface and that of Ni for 10 wt% Ni–$Ce_{0.10}Ti_{0.90}O_2$ seemed to be lowered.

3.1.2 Extended X-ray absorption fine structure (EXAFS) analysis. In this part, data analysis in the region of extended X-ray absorption fine structure was carried out in order to evidence the incorporation of added metals into TiO_2 lattice. In the EXAFS region, the multiscattering peaks occur when the core electron is ejected from the probe atom and is back-scattered by multiple neighboring atoms resulting in constructive interference. Therefore, data concerning the EXAFS region, types of neighboring atom, coordination number and bond length are obtained. Fig. 5(a) illustrates the FT-EXAFS spectra in k-space for TiO_2, 10 wt% Ni–TiO_2 and 10 wt% Ni–
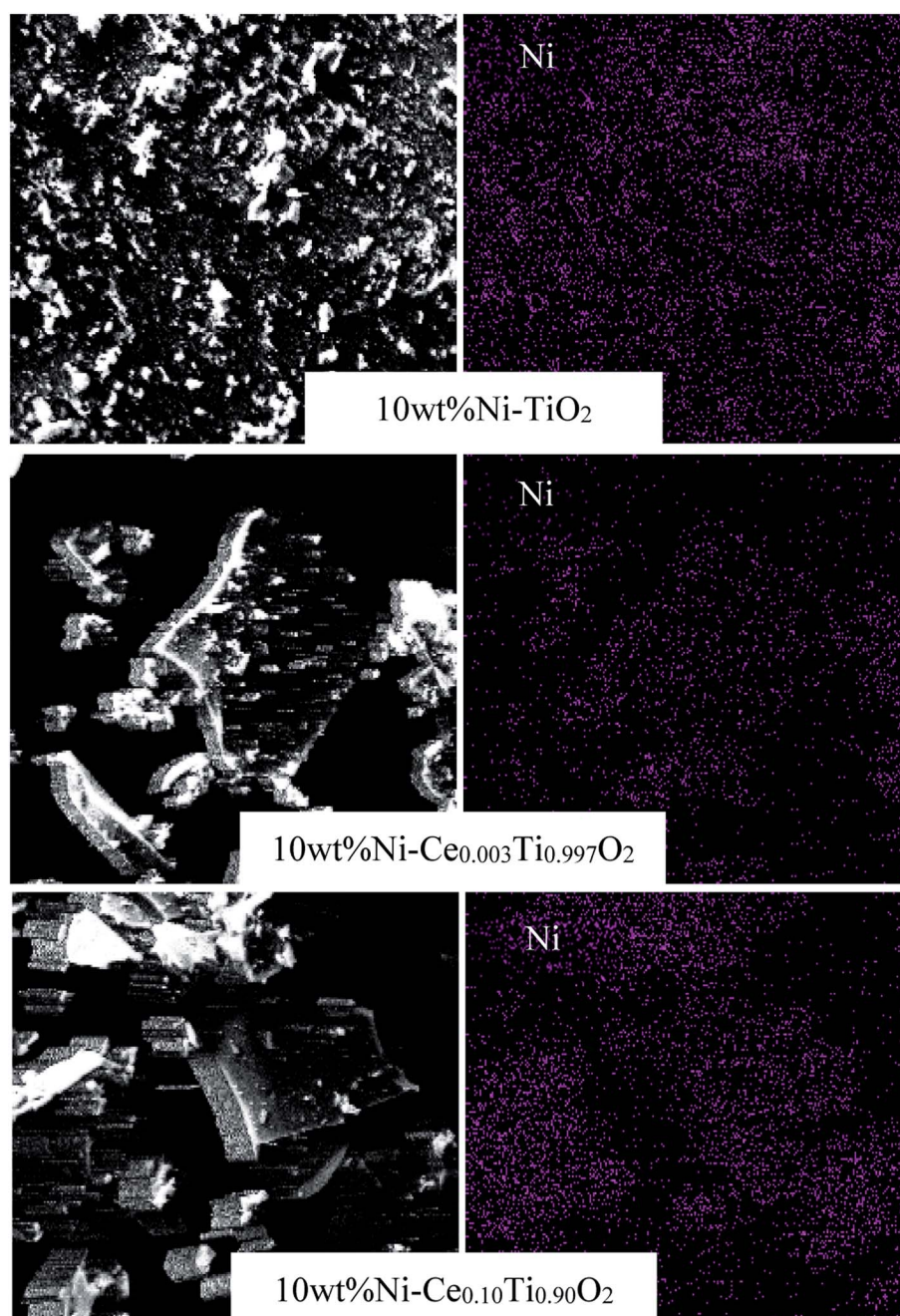

Fig. 4   SEM and mapping images of TiO_2 and 10 wt% Ni–$Ce_xTi_{1-x}O_2$ (x = 0, 0.003 and 0.10) catalysts.

$Ce_{0.003}Ti_{0.997}O_2$ catalysts. The k^2 weighted Fourier transform was used. The weighted EXAFS data in the k range from 3–10.5 Å^{-1} were transformed to R-space without phase correction as shown in Fig. 5(b). The calculated FT-EXAFS of TiO_2 was obtained by fitting with anatase TiO_2 (space group $I4_1/amd$). Similarly, the FT-EXAFS spectrum of 10 wt% Ni–TiO_2 was obtained by replacing one atom of the nearest Ti atom with Ni. For the Ce-doped sample (10 wt% Ni–$Ce_{0.003}Ti_{0.997}O_2$), the FT-EXAFS spectrum was obtained by replacing the nearest Ti atom with one Ni and one Ce atom. For Fig. 5(b), all doped samples exhibited a similar feature of FT-EXAFS spectra to TiO_2 in the range of $R = 1$–4 Å. The first strongest peak was due to a single scattering path of absorbing Ti atoms with the nearest O atoms (Ti–O) by six-fold coordination. The other two peaks in the range of 2–4 Å were attributed from single scattering paths of absorbing atoms with the nearest Ti atoms (Ti–Ti) and with

Table 2 The structural parameters obtained by fitting the EXAFS data

Catalyst	Paths	N	S_0^2	σ^2	R (Å)	R-Factor
TiO_2	Ti–O	4	0.95	0.0243	1.8249	0.0180
		2		0.0002	1.9251	
	Ti–Ti	4		0.0105	3.0337	
		4		0.0099	3.8523	
10 wt% Ni– TiO_2	Ti–O	4	0.72	0.0040	1.9333	0.0064
		2		0.0087	2.4159	
	Ti–Ni	1		0.0002	2.9747	
	Ti–Ti	3		0.0227	3.0211	
		4		0.0084	3.8878	
10 wt% $Ni–Ce_{0.003}Ti_{0.997}O_2$	Ti–O	4	0.65	0.0030	1.9295	0.0061
		2		0.0048	2.4325	
	Ti–Ni	1		0.0025	2.9674	
	Ti–Ce	1		0.0158	2.9892	
	Ti–Ti	2		0.0075	3.0550	
		4		0.00802	3.8954	

the nearest Ni and/or Ce atoms (Ti–Ni, Ti–Ce) for doped samples. Table 2 shows the obtained structural parameters from fitting of TiO_2 and doped catalysts. In the case of Ni-impregnated sample (10 wt% Ni–TiO_2), the expansion of Ti–O and Ti–Ti bond length together with a lowering of Ti–Ni distance when compared with Ti–Ti bond length were observed, which indicated the incorporation of larger Ni^{2+} ions into the TiO_2 lattice. Upon the addition of Ce into the TiO_2 lattice which was impregnated with Ni, expansion of the bond length between Ti–O and Ti–Ti were clearly observed, which indicated that the Ce was incorporated into the TiO_2 lattice. From the EXAFS results, it is confirmed that Ni and Ce were incorporated into the TiO_2 lattice.

3.2 CO_2 methanation catalytic activity study

The catalytic activity of all prepared catalysts was tested for the CO_2 methanation reaction. Before starting the reaction, the catalyst was pretreated at 450 °C under H_2 atmosphere with a flow rate of 50 mL min^{-1} for 1.5 h in order to reduce Ni^{2+} to Ni^0.

After that, the CO_2 methanation reaction was started by switching the feed gas into the reactor. The catalytic activity of the prepared catalysts was studied in the temperature range of 100–500 °C. The percentages of CO_2 conversion for all prepared catalysts are plotted as a function of reaction temperature, as shown in Fig. 6(a). It can be seen that the CO_2 conversion were increased with increased reaction temperature. For TiO_2 catalyst, the CO_2 conversion was very low though the reaction temperature reached 500 °C. Upon doping of Ni onto TiO_2, the CO_2 conversion was dramatically enhanced. It is noteworthy that the incorporation of Ce into the TiO_2 catalyst promoted the CO_2 conversion ability. The results show that 10 wt% Ni–$Ce_{0.003}Ti_{0.997}O_2$ exhibits the highest CO_2 conversion with the maximum value of 65.29% at 450 °C, while increasing the Ce contents led to a decrease in catalytic activities. For the products (CH_4 and CO) yield as illustrated in Fig. SI 1(a) and (b),† it was
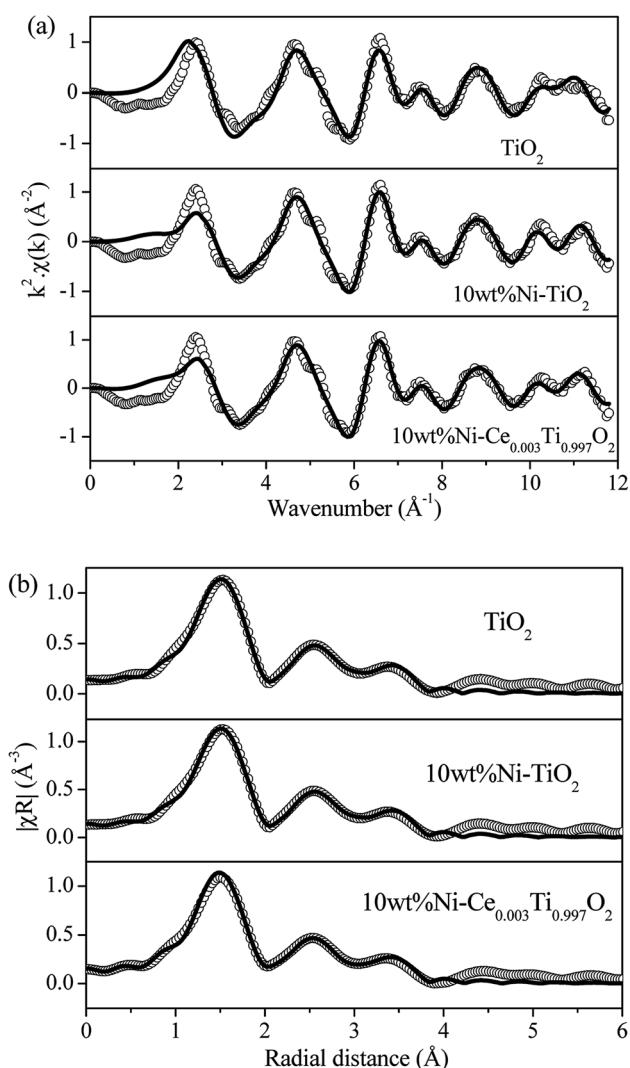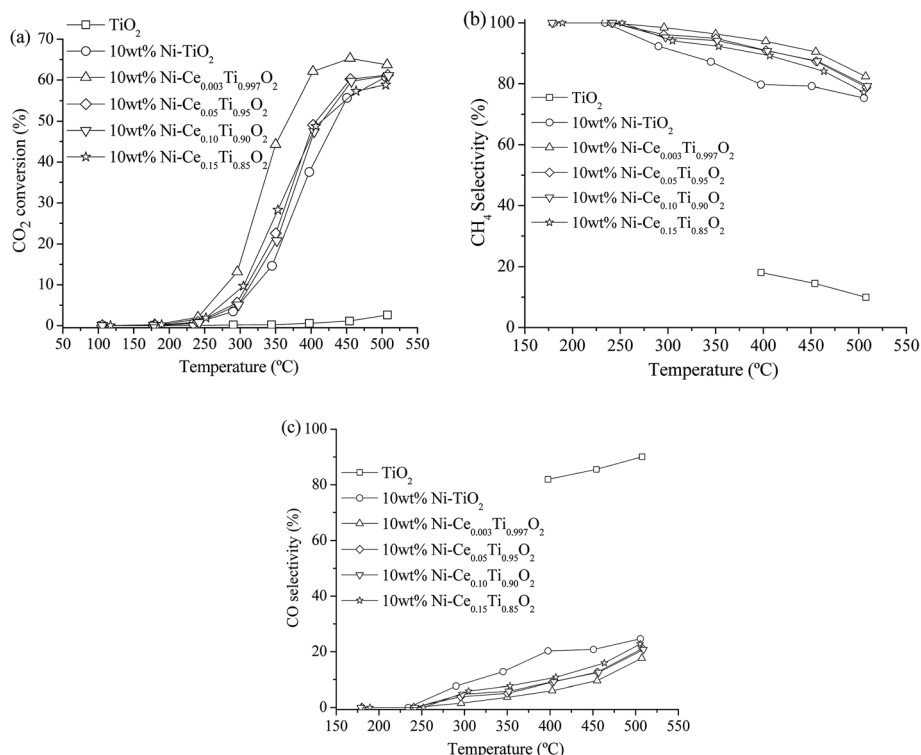

Fig. 5 (a) Experimental (open circle) and calculated (black line) FT-EXAFS spectra in k-space for TiO_2, 10 wt% Ni–TiO_2 and 10 wt% Ni–$Ce_{0.003}Ti_{0.997}O_2$. (b) Experimental (open circle) and calculated (black line) FT-EXAFS spectra in R-space for TiO_2, 10 wt% Ni–TiO_2 and 10 wt% Ni–$Ce_{0.003}Ti_{0.997}O_2$.

Fig. 6 CO_2 conversion (a), CH_4 selectivity (b) and CO selectivity (c) of TiO_2 and 10 wt% $Ni-Ce_xTi_{1-x}O_2$ ($x = 0$, 0.003, 0.05, 0.10 and 0.15) catalysts for CO_2 methanation ($CO_2 : H_2$ ratio = 1 : 4).

found that CH_4 was the main product from CO_2 methanation which produced by Ni-impregnated samples (10 wt% $Ni-TiO_2$ and 10 wt% $Ni-Ce_xTi_{1-x}O_2$, $x = 0.003$, 0.05, 0.10 and 0.15). On the other hand, CO which was produced by reversed water gas shift reaction (side reaction), was the main product for TiO_2 catalyst. Moreover, the CO yield for 10 wt% $Ni-TiO_2$ was higher than that of 10 wt% $Ni-Ce_xTi_{1-x}O_2$ which could indicate that Ce incorporated probably suppressed the formation of undesired product (CO) of this reaction. From Fig. SI 1(b),† it is seen that the CO by-product was favorably enhanced when reaction temperature increase; therefore, the suitable reaction temperature for CO_2 methanation for our reaction condition was 350 °C which exhibited low CO yield with high CO_2 conversion and CH_4 yield. Fig. 6(b) and (c) display the CH_4 and CO selectivities for all synthesized samples. The results show that Ni-

doped on TiO_2 and $Ce_xTi_{1-x}O_2$ catalysts were selectively toward CH_4 while bare TiO_2 catalyst was selectively toward CO. The calculated CO_2 conversion, product yields and product selectivities of all catalysts for CO_2 methanation at 350 °C are summarized in Table 3. In order to evidence that the enhancing of CO_2 methanation rate resulted from Ni and Ce incorporated into TiO_2, NiO and CeO_2 catalysts were also prepared and tested for their catalytic activities. Fig. SI 2(a)–(c)† illustrate the CO_2 conversion, CH_4, and CO yields of NiO and CeO_2 compared with TiO_2 and 10 wt% $Ni-Ce_{0.003}Ti_{0.997}O_2$. It can be seen that NiO and CeO_2 exhibited relatively low CO_2 conversion with low CH_4 and CO yields when compared with the doped sample. Therefore, doped metals into TiO_2 catalyst would play an important role in catalyzing the CO_2 methanation.

Table 3 Percentages of CO_2 conversion, product selectivity, and yield over the prepared catalysts for the CO_2 methanation reaction

Catalyst	CO_2 conversion[a] (%)	Yield[a] (%)		Selectivity[a] (%)		E_a[b] (kJ mol^{-1})
		CO	CH_4	CO	CH_4	
TiO_2	0.22	0.22	0.00	100	—	—
10 wt% $Ni-TiO_2$	14.66	1.87	12.78	12.78	87.22	79.35
10 wt% $Ni-Ce_{0.003}Ti_{0.997}O_2$	44.28	1.62	42.66	3.66	96.34	74.86
10 wt% $Ni-Ce_{0.05}Ti_{0.95}O_2$	22.55	1.14	21.41	5.08	94.92	78.79
10 wt% $Ni-Ce_{0.10}Ti_{0.90}O_2$	20.83	1.22	19.61	5.84	94.16	78.57
10 wt% $Ni-Ce_{0.15}Ti_{0.85}O_2$	28.28	2.18	26.09	7.72	92.28	78.98

[a] Reaction temperature at 350 °C. [b] Calculated by using the temperature range of 230–280 °C (CO_2 conversion less than 15%).
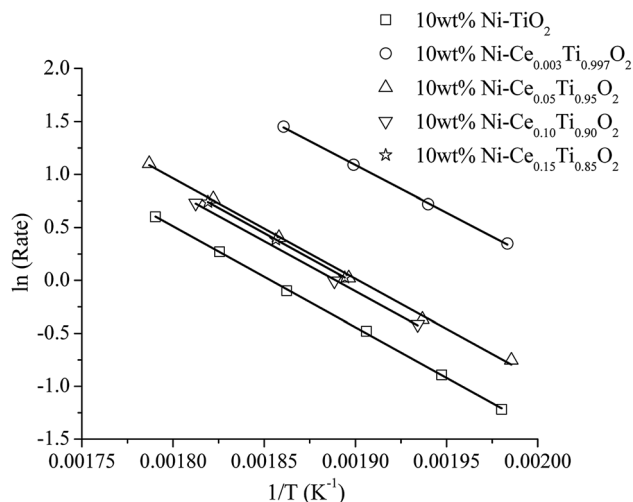
Fig. 7 The Arrhenius plots of 10 wt% $Ni-Ce_xTi_{1-x}O_2$ ($x = 0, 0.003, 0.05, 0.10$ and 0.15) catalysts.

Fig. 8 50 h long-term stability test over 10 wt% $Ni-Ce_{0.003}Ti_{0.997}O_2$ at 350 °C ($CO_2 : H_2$ ratio = 1 : 4).

In order to illustrate the role of the catalysts in enhancing the reaction rate at low temperature, the kinetic study in a term of apparent activation energy (E_a) was carried out. The absence of heat and mass transfer were evidenced as mentioned in experimental part. To determine the apparent activation energy, an Arrhenius plot was constructed. This plot is a relationship between ln(rate) and the reciprocal of absolute temperature corresponding to the Arrhenius equation as presented in eqn (6)

$$k = A \exp\left(\frac{-E_a}{RT}\right) \tag{6}$$

where k is the rate constant, A is the pre-exponential factor, E_a is the activation energy of the reaction, T is the absolute temperature and R is the gas constant (8.314 J K^{-1} mol^{-1}). The apparent activation energies of reactions can be calculated from the slope of the Arrhenius plot. Fig. 7 illustrates the Arrhenius plot of Ni-doped samples and the calculated apparent activation energies were summarized in Table 3.

It can be seen that the activation energy of TiO_2 could not be determined at low temperature because CO_2 conversion was very low. The activation energies of the prepared catalysts appeared in the range of 75–80 kJ mol^{-1}. The apparent activation energies were decreased with the incorporation of Ce into TiO_2 and 10 wt% $Ni-Ce_{0.003}Ti_{0.997}O_2$ exhibits the lowest apparent activation energy which is in agreement with the highest catalytic activity for CO_2 methanation.

The long-term stability of the catalyst is also an important property for CO_2 methanation because metallic Ni can be sintered under exothermic reaction conditions and carbon deposition can also formed on the catalysts surface which can lead to fast deactivation. In this work, a long-term stability test of the best catalyst (10 wt% $Ni-Ce_{0.003}Ti_{0.997}O_2$) was investigated at 350 °C for 50 h. Fig. 8 displays the percentages of CO_2 conversion, CH_4 yield, and selectivity for the reaction time of 50 h. It can be seen that the catalyst exhibited greatly stable CO_2 conversion, CH_4 yield, and selectivity within the whole
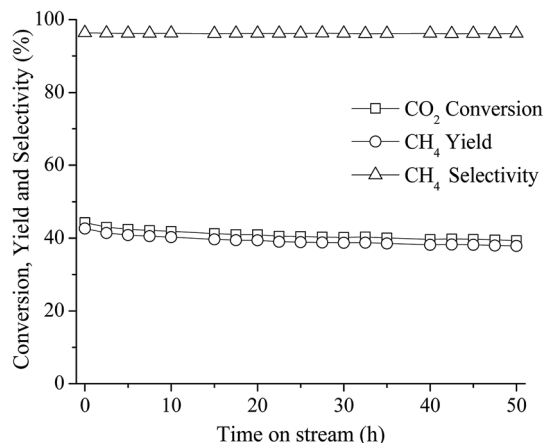
range of stability test (50 h) without an obvious decrease of those values.

To explain the excellent stability under feed stream of this catalyst at this reaction temperature (350 °C), TEM images of used catalysts at interval reaction temperatures (250 °C, 350 °C and 450 °C) were compared. Fig. 9(a) displays TEM images of 10 wt% $Ni-Ce_{0.003}Ti_{0.997}O_2$ catalyst after reaction at 250 °C, 350 °C and 450 °C. The results show that the mean particle sizes of this catalyst after all reaction temperatures were in the rage of 10–12 nm. Agglomeration of particles upon increased of reaction temperature was not observed which indicated that the thermal sintering of the metallic Ni was inhibited.[50] Moreover, carbon deposition on catalyst surface was not also observed (form EDX results). Therefore, from this behaviour, this catalyst exhibited an excellent stability under feed stream with high CH_4 yield and selectivity.

3.3 X-ray absorption spectroscopy (XAS)

X-ray absorption spectroscopy (XAS) technique is used to investigate the electronic states of probe elements in the catalyst. X-ray absorption is the process in which X-ray radiation excites an electron in a core level of an absorbing atom to empty level or is ejected from the atom as a photoelectron. The absorption coefficient of probe atom as a function of excited photon energy is recorded and the plot between these two parameters is called XAS spectrum. The XAS spectrum can be divided into two regions; X-ray absorption near edge structure (XANES) and extended X-ray absorption fine structure (EXAFS). Information on the oxidation state is obtained from the XANES region while the information about types of neighboring atom, coordination number and bond length are obtained from the EXAFS region. In this work, we used XAS technique for (i) evidence of the oxidation state and local structure of the catalyst and (ii) monitoring the catalyst changing during CO_2 methanation reaction.

3.3.1 XANES analysis for electronic structure change and oxidation state determination by *ex situ* experiment. It is worth mentioning that in an XAS experiment, a high probe element content is needed in order to obtain a reasonable spectrum. Since
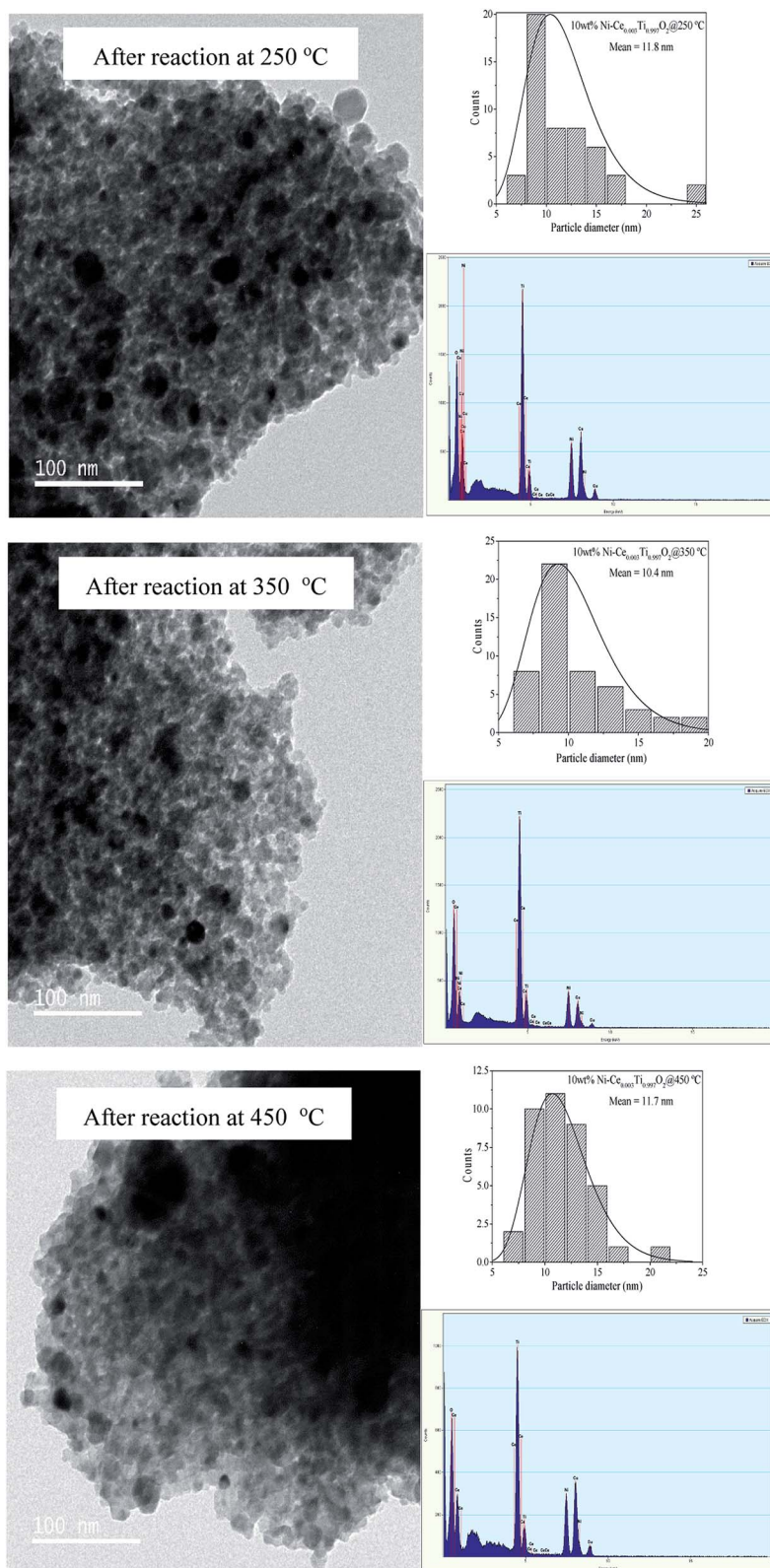
Fig. 9 TEM images of 10 wt% Ni−Ce$_{0.003}$Ti$_{0.997}$O$_2$ after reaction at 250, 350 and 450 °C.

this technique is not sensitive to low metal content and the best catalyst consisted of only 0.24 Ce mole percentage, thus in this part the metal content used in XAS studied was higher (4.11 Ce mole percentage) than of optimal metal content of the catalyst.

In this part, the freshly prepared, pretreated and used catalysts were employed to test for XANES experiment in order to investigate the oxidation states of Ti, Ni and Ce probe atoms in different states of catalysts. Data analysis from XANES spectra

can provide a good deal of useful information such as electronic states, electronic structure and electron density. It is known that the XANES spectra feature in the pre-edge region are sensitive to the electronic structure and crystal structure changing in the materials.[51,52] These changes were monitored to study the influence of metal substitution into TiO_2 by Ni and Ce. Fig. 10(a) illustrates the Ti K edge in the pre-edge region for freshly prepared TiO_2, 10 wt% Ni–TiO_2 and 10 wt% Ni–$Ce_{0.05}Ti_{0.95}O_2$ catalysts. There are three main peaks in pre-edge region; A_1, A_2 and A_3. Feature A_1 is attributed from transition of 1s → 3d-t_{2g} state. Feature A_2 and A_3 resulted from excitation of 1s electron to hybridized p–d (t_{2g}) and p–d (e_g) on the Ti central atom, respectively.[53,54] These three pre-edge peaks intensities were related to the symmetry of the crystal structure. A distortion and oxygen vacancies can cause an increase in the pre-edge intensity.[55,56] From Fig. 10(a), the pre-edge intensity was increased upon the addition of 10 wt% Ni onto TiO_2 which was due to an incorporation of Ni into TiO_2 lattice. In addition, these pre-edge peaks intensities were further increased when Ce addition for 10 wt% Ni–$Ce_{0.05}Ti_{0.95}O_2$ catalyst. This indicated that Ce was further incorporated into TiO_2 lattice and led to more defects and oxygen vacancies in the doped catalyst. Fig. 10(b) and (c) show a comparison between Ni^0 and Ni^{2+} standards with three different catalysts for 10 wt% Ni–TiO_2 and 10 wt% Ni–$Ce_{0.05}Ti_{0.95}O_2$, respectively. For NiO standard, the white line peak at 8350 eV was observed which is attributed to the transition from 1s to the unoccupied 4p state and the other peak at 8366 eV was a signature of Ni in 6-fold coordinated by O atoms.[57–59] The Ni foil spectrum exhibits a shoulder at around

8334 eV which is assigned to the electron transition from 1s to 3d orbital.[60] Comparison between the XANES spectra of standards and samples can initially indicate the oxidation states of the probe atom. However, from our result, the XANES spectra of all samples were not completely identical to both standards. Therefore, the oxidation state of samples cannot be estimated by only comparison with standard spectra. For this aspect, the apparent oxidation state of Ni should be determined. To confirm the apparent oxidation states of the probe atom (Ni), the relationship between the Ni K edge energy of different samples relative to the edge energy of Ni metal (ΔE) and oxidation state of Ni was constructed as shown in Fig. SI 3(a) and (b).† For both 10 wt% Ni–TiO_2 and 10 wt% Ni–$Ce_{0.05}Ti_{0.95}O_2$, the Ni oxidation state of freshly prepared catalyst was Ni^{2+} while pretreated and used samples were close to Ni^0. It is seen that the reduction of Ni^{2+} was not completed to Ni^0 which was probably due to the oxidation of some Ni species on the catalyst when exposed in air, since these catalysts (pretreated and used catalysts) were obtained after those steps in the catalytic activity process.

Fig. 10(d) illustrates Ce L_3 edge XANES spectra of three different types of 10 wt% Ni–$Ce_{0.05}Ti_{0.95}O_2$ comparing with Ce^{3+} and Ce^{4+} standards. For $Ce(NO_3)_3 \cdot 6H_2O$ (Ce^{3+}) standard, a single white line, labeled as B_0, is assigned as the transition of an electron from Ce core $2p_{3/2}$ state to $4f^1 5d$ state. For CeO_2 (Ce^{4+}) standard, two peaks were observed. These two peaks (labeled as B_1 and C) are attributed to electron transition from Ce $2p_{3/2}$ to a final state with the configuration of $4f^1 5d$ and $4f^0 5d$.[61,62] For Ce^{3+}, the transition of an electron from Ce $2p_{3/2}$ to
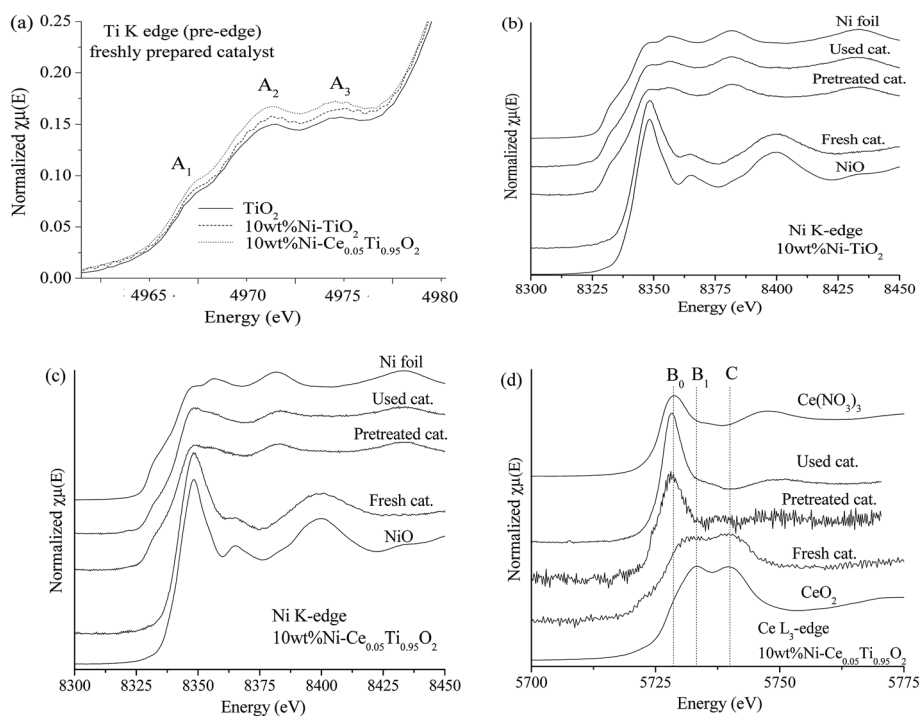

Fig. 10 (a) The Ti K edge XANES spectra in the pre-edge region of fresh TiO_2, 10 wt% Ni–TiO_2 and 10 wt% Ni–$Ce_{0.05}Ti_{0.95}O_2$ catalysts. The Ni K edge XANES spectra of fresh, pretreated and used 10 wt% Ni–TiO_2 (b) and 10 wt% Ni–$Ce_{0.05}Ti_{0.95}O_2$ (c) catalysts. (d) The Ce L_3 edge XANES spectra of fresh, pretreated and used 10 wt% Ni–$Ce_{0.05}Ti_{0.95}O_2$ catalyst.
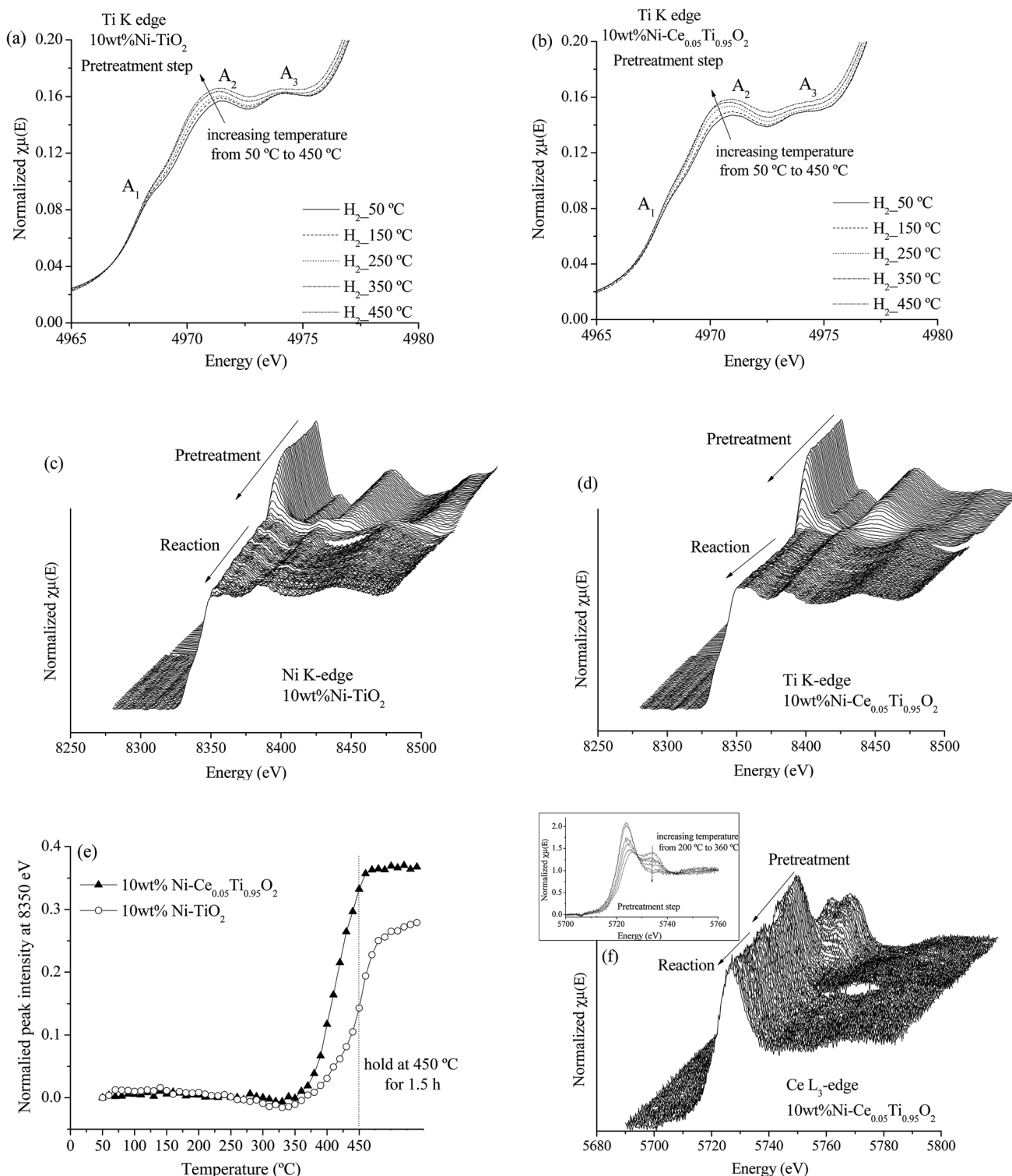
Fig. 11　Ti K edge XANES in the pre-edge region during pretreatment step for 10 wt% Ni–TiO$_2$ (a) and 10 wt% Ni–Ce$_{0.05}$Ti$_{0.95}$O$_2$ (b). Ni K edge XANES spectra during pretreatment and CO$_2$ methanation reaction for 10 wt% Ni–TiO$_2$ (c) and 10 wt% Ni–Ce$_{0.05}$Ti$_{0.95}$O$_2$ (d). (e) The normalized peak intensity at 8350 eV from Ni K edge XANES spectra as a function of pretreated temperature for 10 wt% Ni–TiO$_2$ and 10 wt% Ni–Ce$_{0.05}$Ti$_{0.95}$O$_2$. (f) Ce L$_3$ edge XANES spectra during pretreatment and CO$_2$ methanation reaction for 10 wt% Ni–Ce$_{0.05}$Ti$_{0.95}$O$_2$ (inset; Ce L$_3$ edge XANES spectra during pretreatment step).

an empty 5d state in which the 4f valence state of Ce is occupied by a single electron occurred, while for Ce^{4+}, the 4f state is formally unoccupied, but it can borrow an electron from its oxygen neighbors; thus Ce^{4+} exhibits a mixed-valence state during the exchange of electrons. For freshly prepared catalysts, the XANES spectrum feature was similar to that of CeO$_2$. Upon

being pretreated by H_2 and after the reaction, the XANES spectra were quite similar to Ce^{3+} standard. Fig. SI 3(c)† shows that the apparent oxidation state of freshly prepared 10 wt% Ni–$Ce_{0.05}Ti_{0.95}O_2$ was lower than 4+ which indicated a mixing between some Ce^{3+} and Ce^{4+} in the sample. While for pretreated and used catalysts, the oxidation state of Ce was lower than that of freshly prepared catalyst and quite close to Ce^{3+} which was due to the reduction of Ce^{4+} to Ce^{3+} under H_2 atmosphere.

3.3.2 *In situ* experiment for monitoring the changing of catalyst states during CO_2 methanation.

In previous *ex situ* experiments, three different catalysts which were obtained after preparation, after pretreatment by H_2 and after CO_2 methanation reaction were studied. Therefore, the oxidation states of catalysts for each step were determined. In this part, the prepared catalysts were employed to study the oxidation state changing of Ti, Ni and Ce during the reaction. As discussed in previous part, added metal into TiO_2 would lead to some structural changing and defect sites in TiO_2. The structural changing around Ti for 10 wt% Ni–TiO_2 and 10 wt% Ni–$Ce_{0.05}Ti_{0.95}O_2$ can be observed by using pre-edge region during pretreatment step as illustrated in Fig. 11(a) and (b). For both samples, increasing the reduction temperature (under H_2 atmosphere) led to an increase of pre-edge peak intensities which indicated to higher disorder or more oxygen vacancies around Ti absorbing atoms.

Fig. 11(c) and (d) illustrate the Ni K edge XANES spectra of Ni-impregnated on TiO_2 and $Ce_{0.05}Ti_{0.95}O_2$ catalysts. These two catalysts exhibit the same changing of XANES spectra during two steps. For the pretreatment step, the oxidation state of Ni was changed from Ni^{2+} (initial state for pretreated catalyst) to Ni^0 with increased temperature from 50–450 °C. Note that, in the *in situ* experiment, Ni^{2+} was completely reduced to Ni^0 as shown in Fig. SI 4,† since the sample was performed under H_2 atmosphere. However, the starting reduction temperature of these two samples were different. Fig. 11(e) shows the different starting reduction temperatures of both samples. The plot was expressed as normalized peak intensity at 8350 eV (white line position of Ni^{2+}) as a function of temperature. The normalized peak intensity was calculated from the difference between peak intensity at 8350 eV of the initial state and that of each temperature divided by peak intensity at the initial state. Therefore, an increase of this value indicated a lowering of the white line intensity of Ni^{2+}, *i.e.*, Ni^{2+} was reduced to Ni^0. From Fig. 11(e), the starting reduction temperature of 10 wt% Ni–TiO_2 was higher than that of 10 wt% Ni–$Ce_{0.05}Ti_{0.95}O_2$. This result can indicate an improvement of reducibility of Ce-doped catalyst which could alter its catalytic activity. In addition, under CO_2 methanation conditions, the oxidation states of Ni for both catalysts remained unchanged from the initial state (Ni^0 after pretreatment step). Fig. 11(f) shows Ce L_3 edge XANES spectra of 10 wt% Ni–$Ce_{0.05}Ti_{0.95}O_2$ during pretreatment and CO_2 methanation reaction. It can be seen that the oxidation state changing of Ce^{4+} to Ce^{3+} during the pretreatment process occurred. The Ce^{4+} was started to reduce at the reduction temperature around 220 °C and completely reduced to Ce^{3+} at around 360 °C (as shown in the inset). After that, the oxidation state of Ce was not changed during the reaction. From the above results, it can be

summarized that (1) the changing of environmental structure around Ti during the pretreatment process was found which in accordance with the changing of Ce oxidation state from Ce^{4+} to Ce^{3+}. Due to the incorporation of Ce into TiO_2 lattice, the oxygen vacancies or defect sites existent upon Ce modification was observed, (2) for Ni oxidation state change, the reduction of Ni^{2+} to Ni^0 at lower temperature upon the addition of Ce into the catalyst could be used to describe the enhancing of CO_2 methanation activity for the Ce-doped sample.

3.3.3 *In situ* Ni K-edge EXAFS spectra under CO_2 methanation conditions.

The Ni K-edge EXAFS spectra were used to monitor the structural changing of 10 wt% Ni–$Ce_{0.003}Ti_{0.997}O_2$ catalyst under CO_2 methanation reaction. Fig. 12(a) reveals the EXAFS spectra in *R*-space of Ni foil and 10 wt% Ni–$Ce_{0.003}Ti_{0.997}O_2$ catalysts at the reaction temperature of 100, 350 and 550 °C. It can be seen that the feature of EXAFS spectra for all reaction temperature was similar to Ni foil. However, the amplitude of the spectra decreased with increased of reaction temperature. Since the amplitude of EXAFS spectra corresponded to the coordination number, therefore, the EXAFS spectra fitting was done in order to obtain the information on the coordination number around Ni absorbing atoms and explain the reduction of EXAFS amplitude during the CO_2 methanation reaction. The experimental and calculated k^2 weighted Ni K-edge EXAFS spectra of the Ni foil standard and 10 wt% Ni–$Ce_{0.003}Ti_{0.997}O_2$ catalysts at 100, 350 and 550 °C are shown in Fig. 12(b). The k^2 weighted EXAFS data from Fig. 12(b) was transformed to *R*-space without phase correction (Fig. 12(c)). The calculated EXAFS of all samples was obtained by fitting the cubic close-packed (ccp) Ni structure (space group $Fm\bar{3}m$) from the databases with experimental EXAFS data by using the Artemis program. The structural parameters from EXAFS fitting are summarized in Table 4 which presented the coordination number (N), radial distance (R) between absorbing Ni atoms with neighboring Ni atoms, Debye–Waller factor (σ^2) and *R*-factor. The fitting results exhibited that a first strong peak at around 2.0 Å (2.48 Å from fitting) indicated a single scattering path of absorbing Ni atom with the nearest neighboring Ni atoms (Ni–Ni). For Ni foil standard, the calculated coordination number was 12 which indicated that the absorbing Ni atom was surrounded by 12 neighboring Ni atoms. However, the calculated coordination number of 10 wt% Ni–$Ce_{0.003}Ti_{0.997}O_2$ catalyst at 100, 350 and 550 °C decreased to 9.3, 8.4 and 5.3, respectively. The lowering of Ni–Ni coordination numbers at higher temperatures, *i.e.*, Ni–Ni coordination number at 100 °C = 9.3 and at 550 °C = 5.3; indicated a higher unsaturated Ni–Ni coordination number. High unsaturated numbers of Ni species can lead to existing more active site/defect and can accelerate the dissociative adsorption for H_2 to involve in the reaction.[14,63] Moreover, the Debye–Waller factor of Ni–Ni pairs increased when the reaction temperature increased. This indicated the deviation of the Ni atom position from the cubic close-packed (ccp) Ni structure due to the more vibration of atoms at high temperature. This result is in agreement with Liu *et al.*[64]

However, the H_2 adsorption ability on an active site was one of the main factor to describe the catalytic performance. Therefore, to explain the catalytic activities enhancement,
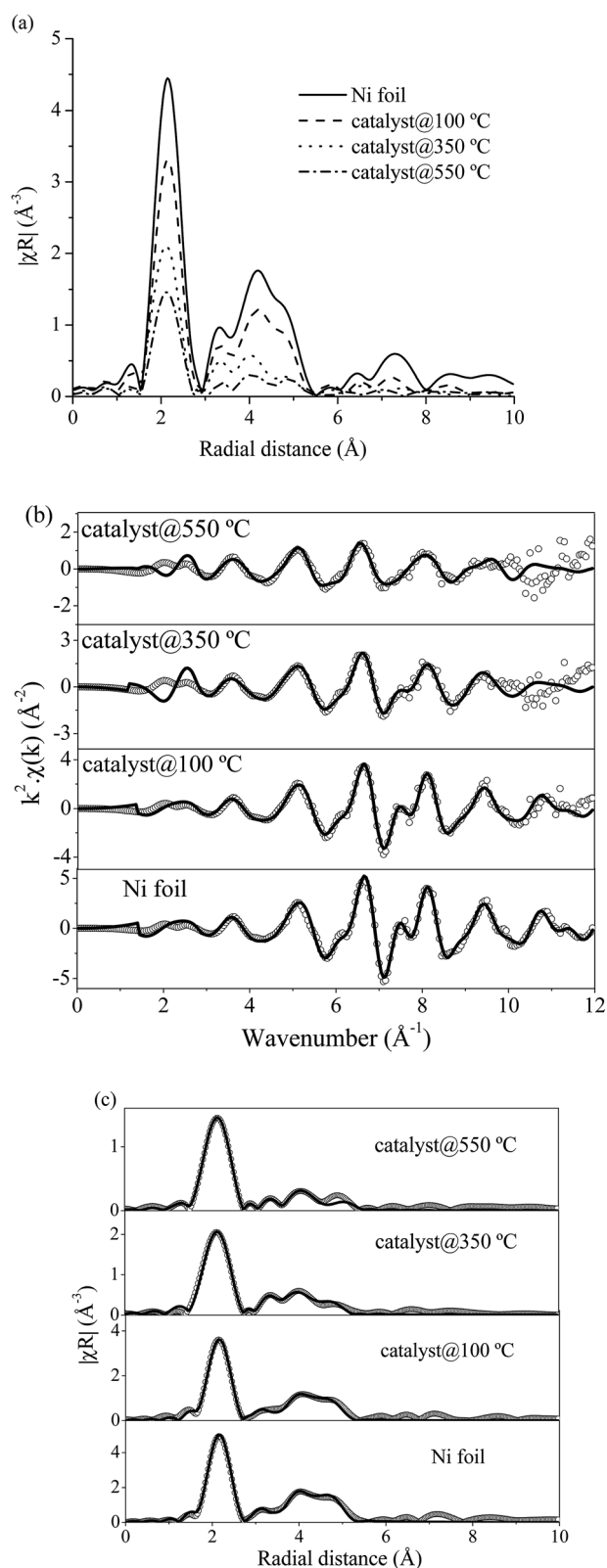
Fig. 12 (a) Normalized Ni K-edge EXAFS spectra in R space of Ni foil and 10 wt% Ni–Ce$_{0.003}$Ti$_{0.997}$O$_2$ catalyst at reaction temperature of 100, 350 and 550 °C. (b) Experimental (open circle) and calculated (black line) FT-EXAFS spectra in k-space of Ni foil and 10 wt% Ni–Ce$_{0.003}$Ti$_{0.997}$O$_2$ catalyst at reaction temperature of 100, 350 and 550 °C. (c) Experimental (open circle) and calculated (black line) FT-EXAFS spectra in R-space of Ni foil and 10 wt% Ni–Ce$_{0.003}$Ti$_{0.997}$O$_2$ catalysts at reaction temperature of 100, 350 and 550 °C.

understanding on the adsorption behavior of two reactants should be investigated.

3.4 The role of Ce addition on TiO$_2$-supported Ni catalyst on enhancing CO$_2$ methanation

It is known that many properties such as surface properties (surface area, pore size and volume), electrical, structural and redox properties can dominate the catalytic activities of the catalysts. In this work, Ce was added into TiO$_2$-supported Ni to improve the catalytic activity for CO$_2$ methanation reaction. The results showed that the catalytic activity of TiO$_2$-supported Ni was significantly increased upon addition of small amount of Ce (0.003 mol%). It is noted that Ni species can facilitate the dissociative-adsorption of H$_2$ molecules and, in this work, the amounts of impregnated Ni were similar for all doped catalysts (10 wt% Ni); thus, the difference of catalytic activities of samples with different amounts of Ce should be resulted from the effects of Ce addition. Therefore, it is implied that the addition of Ce would lead to improvement of some catalyst properties which were already characterized and investigated by several techniques.

In this part, the effects of Ce addition on TiO$_2$-supported Ni catalytic activity for CO$_2$ methanation are summarized.

(1) Addition of Ce improved the dispersion of Ni on catalyst surface. The results from SEM and mapping images in characterization section indicated that the dispersion of Ni on catalysts surface was improved upon addition of Ce when compared with that of Ni on bare TiO$_2$ without Ce addition. Moreover, the highest Ni dispersion was obtained by addition of small amount of Ce (0.003 mol%). It is known that H$_2$ molecules favor to adsorb on metallic surface (Ni^0) in dissociative paths, $i.e.$, H$_2$ dissociative adsorption occurs in H atoms formed on metallic surface. Then the dissociated H atoms were further involved in the reaction of CO$_2$ methanation. Therefore, larger area of Ni active metal would lead to larger amount of dissociated H atoms to be involved in the reaction pathways. In order to evidence the role of Ni active metal area on enhancing the catalytic activity, the H$_2$ adsorption experiment on all synthesized catalysts was conducted. Fig. 13 illustrates the H$_2$ adsorption capacity at room temperature for 4 h of all prepared catalysts. From Fig. 13, it can be seen that the lowest H$_2$ adsorption capacity can be observed on the TiO$_2$ surface while the H$_2$ adsorption capacity increased when Ni was added. The role of Ni sites on H$_2$ adsorption has been reported by many research groups.[2,65,66] It is due to Ni on the catalyst surface acting as the active species for H$_2$ adsorption by dissociation of H$_2$ to form atomic H, in which atomic H facilitates the methane formation. From this results, the highest H$_2$ adsorption capacity was observed for 10 wt% Ni–Ce$_{0.003}$Ti$_{0.997}$O$_2$ which exhibited the highest Ni dispersion among all Ce doped catalysts. Therefore, the catalyst with the lowest Ce amount trended to exhibit the highest CO$_2$ methanation activity. Moreover, Ce addition can also promote the stability of catalyst by prevent the sintering of catalyst and also exhibited coking deposition inhibition.

(2) Ce addition can produce the oxygen vacancies within TiO$_2$ lattice. The results from XRD analysis, addition of Ni led to an

Table 4 The structural parameters obtained from the fitting of the EXAFS data for 10 wt% Ni–Ce$_{0.003}$Ti$_{0.997}$O$_2$ during CO$_2$ methanation

Catalyst	Path	EXAFS best fit parameters			
		N	σ^2	R (Å)	R-Factor
Ni foil	Ni–Ni	12.0	0.0071	2.48	0.0055
10 wt% Ni–Ce$_{0.003}$Ti$_{0.997}$O$_2$ at 100 °C	Ni–Ni	9.3	0.0073	2.48	0.0080
10 wt% Ni–Ce$_{0.003}$Ti$_{0.997}$O$_2$ at 350 °C	Ni–Ni	8.4	0.0105	2.48	0.0074
10 wt% Ni–Ce$_{0.003}$Ti$_{0.997}$O$_2$ at 550 °C	Ni–Ni	5.3	0.0106	2.48	0.0028
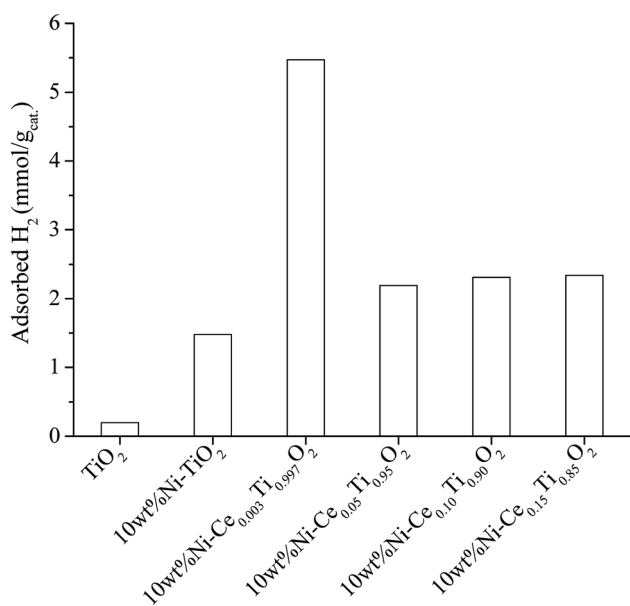
Fig. 13 H$_2$ adsorption result of TiO$_2$ and 10 wt% Ni–Ce$_x$Ti$_{1-x}$O$_2$ ($x = 0$, 0.003, 0.05, 0.10 and 0.15) catalysts.

enlargement of TiO$_2$ unit cell and further increased of unit cell of TiO$_2$ was observed upon increased of Ce loading. Therefore, addition of these two metals led to producing defects or oxygen vacancies within TiO$_2$ lattice. These structural changes were due to the incorporation of larger added metal ions into TiO$_2$ lattice (perhaps interstitial site or by replacing Ti^{4+} site). Moreover, another result that confirmed this structural modification was an XANES and EXAFS of Ti K edge which indicated the distortion of environmental neighboring atoms around the Ti probe atom upon the addition of Ni and Ce. However, the structural change of Ti obtained from XAS was too small to observe, which could be due to the lower amount of added metals when compared with the amount of bulk Ti in the catalyst, where the XAS technique was a bulk technique. Therefore, in order to evidence the incorporation of added metals into TiO$_2$ lattice which can produce the Ti^{3+} (oxygen vacancies) on a catalyst, X-ray photoelectron spectroscopy (XPS), which was a surface sensitive technique was used. Fig. 14(a)–(c) reveal Ti 2p XPS spectra of TiO$_2$, 10 wt% Ni–TiO$_2$, and 10 wt% Ni–Ce$_{0.003}$Ti$_{0.997}$O$_2$, respectively. The obtained XPS peak of the catalyst was analyzed by the fitting of XPS peaks with Gaussian–Lorentzian peaks after the subtraction of a Shirley background

using the XPSPEAK41 program. The information from fitting include the peak position and peak area. The oxidation state of Ti in the catalysts can be obtained by comparing the peak position from fitting with the peak position of references. It can be seen that Ti 2p XPS spectra of TiO$_2$ in Fig. 14(a) exhibits two peaks at around 458 and 464 eV corresponding to the electron transition of Ti^{4+} from 2p$_{3/2}$ and 2p$_{1/2}$ to form a photoelectron. For XPS spectra of 10 wt% Ni–TiO$_2$ (Fig. 14(b)) and 10 wt% Ni–Ce$_{0.003}$Ti$_{0.997}$O$_2$ (Fig. 14(c)) catalysts, four XPS peaks can be observed. The two XPS peaks at around 458 and 464 eV were the characteristic of Ti^{4+} species while another two peaks at around 456 and 462 eV were the electron transition from 2p$_{3/2}$ and 2p$_{1/2}$ for Ti^{3+} species. Therefore, Ti composition of Ni and Ce co-added catalysts contained the mixing of Ti^{4+} and Ti^{3+} species on the surface. The presence of Ti^{3+} in the catalyst structure indicated the formation of oxygen vacancies on the catalyst surface.[67] However, the Ti^{3+}/Ti^{4+} XPS peak area ratio of 10 wt% Ni–Ce$_{0.003}$Ti$_{0.997}$O$_2$ was higher than that of 10 wt% Ni–TiO$_2$ which indicated that higher oxygen vacancies sites than that of 10 wt% Ni–TiO$_2$. The oxygen vacancies are the active species for CO$_2$ adsorption which interacts with the oxygen of CO$_2$ molecules by strong interaction and weakened the C=O bond.[50,65,68] The oxygen vacancies for CO$_2$ adsorption can be generated by some Ti^{4+} being substituted by metal with a lower oxidation state (Ce^{3+} and Ni^{2+}) and some Ti^{4+} being transformed to Ti^{3+} and then oxygen atoms were lost from the catalyst structure.

Beside the existence of oxygen vacancies that can affect CO$_2$ adsorption, the addition of Ce into TiO$_2$ also increased CO$_2$ uptake by creating a basicity site. Due to weak acidic properties of CO$_2$, increasing the basicity of the catalyst can also improve the adsorption of CO$_2$. Many works have reported on increasing catalyst basicity by adding some metal oxide, such as La$_2$O$_3$ and MgO.[69,70] Therefore, in order to evidence the improvement of basicity of catalysts, a CO$_2$ adsorption experiment under ambient pressure and temperature was carried out. To investigate the CO$_2$ adsorption efficiency of the prepared catalysts, diluted CO$_2$ was injected to the catalysts and kept at room temperature (298 K) for 4 h. After that, the amount of unadsorbed CO$_2$ was detected by Micro GC every 30 min. Fig. 15 reveals time-dependent CO$_2$ adsorption of all the prepared catalysts. It can be seen that CO$_2$ adsorption of all prepared catalysts reached the equilibrium point within 1 h. The CO$_2$ adsorption capacity (mmol of CO$_2$ per g of catalyst) of TiO$_2$ showed the lowest capacity, while the CO$_2$ adsorption capacity increased upon adding Ni metal in TiO$_2$ and further increased
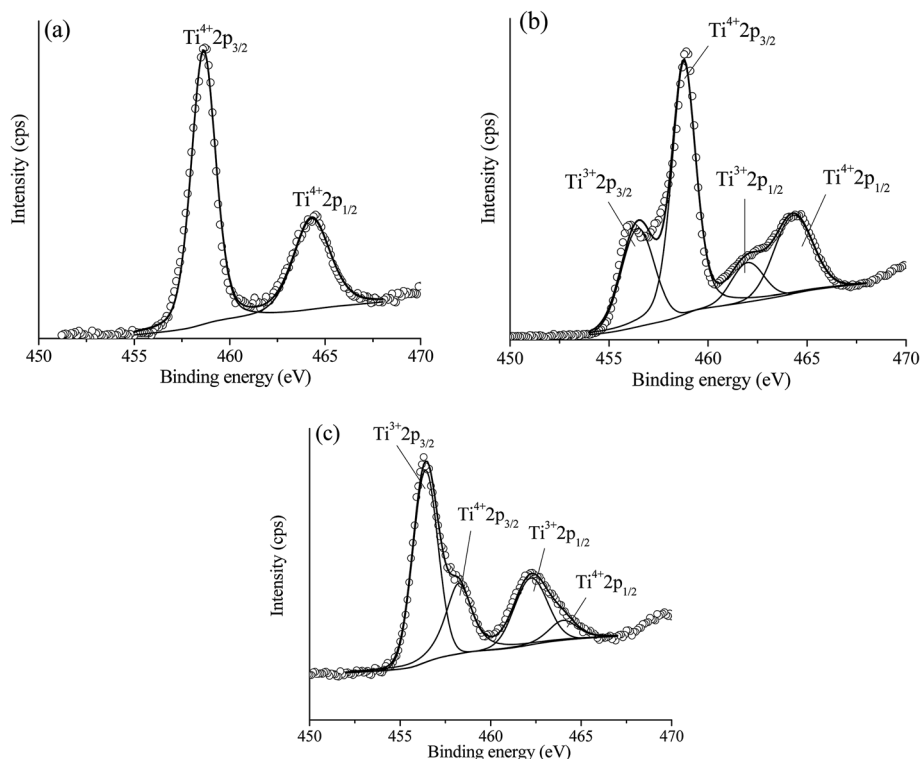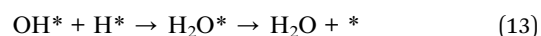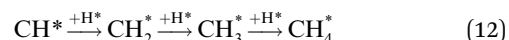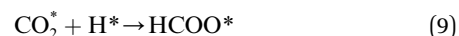
Fig. 14 Experimental (open circle) and calculated (black line) Ti 2p XPS spectra of TiO_2 (a), 10 wt% Ni–TiO_2 (b) and 10 wt% Ni–$Ce_{0.003}Ti_{0.997}O_2$ (c).

with an increase of Ce content. The catalysts with the highest Ce amount exhibited the maximum CO_2 adsorption capacity, which is probably due to the highest basicity. However, the trend of increasing CO_2 uptake with increased Ce content was not related to the catalytic activities results. Therefore, it indicated that CO_2 adsorption ability was not the main factor to enhance the reaction rate.

(3) Ce addition can alter the reducibility of catalysts. Higher reducibility of Ce-doped catalysts can be evidenced by *in situ* XANES results for Ni K edge, which revealed that the starting reduction temperature of 10 wt% Ni–$Ce_{0.05}Ti_{0.95}O_2$ exhibited a lower reduction temperature of $Ni^{2+} \rightarrow Ni^0$. This lowering of

reduction temperature can indicate that the reduction of Ni^{2+} was facilitated by the addition of Ce to improve the reducibility of the catalyst which can lead to more effectively catalyzation of the reaction, as mentioned by other works.[26,71,72]

The CO_2 methanation reaction involved the interaction between CO_2 and H_2 molecule on the catalyst surface. Several pathways of the CO_2 methanation mechanism on the catalyst surface have been proposed by many research groups. Ren *et al.*[73] proposed one of the mechanisms for CO_2 methanation as follows:

$$H_2 + 2* \rightarrow 2H* \tag{7}$$

$$CO_2 + * \rightarrow CO_2^* \tag{8}$$

$$CO_2^* + H* \rightarrow HCOO* \tag{9}$$

$$HCOO* \rightarrow CO* + OH* \tag{10}$$

$$CO* + 2H* \rightarrow CH* + OH* \tag{11}$$

$$CH* \xrightarrow{+H*} CH_2^* \xrightarrow{+H*} CH_3^* \xrightarrow{+H*} CH_4^* \tag{12}$$

$$OH* + H* \rightarrow H_2O* \rightarrow H_2O + * \tag{13}$$

where * represents active sites that interact with the species. From the above equation, it can be seen that the first step that improves the catalytic activity of the catalyst for CO_2 methanation is to facilitate the H_2 and CO_2 adsorption at the active sites on the catalyst. It means that if H_2 and CO_2 molecules are
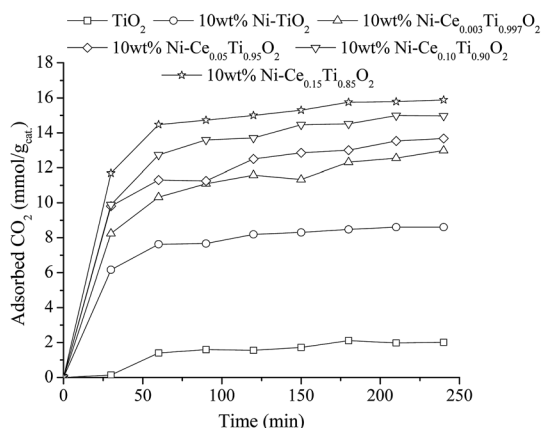

Fig. 15 CO_2 adsorption result of TiO_2 and 10 wt% Ni–$Ce_xTi_{1-x}O_2$ ($x =$ 0, 0.003, 0.05, 0.10 and 0.15) catalysts.

adsorbed on the surface of the catalyst with high efficiency, the catalyst also exhibits high catalytic activity for CO_2 methanation. In this work, we investigated the ability of prepared catalyst for CO_2 and H_2 adsorption. The results exhibited that 10 wt% Ni–$Ce_{0.15}Ti_{0.85}O_2$ displayed the highest CO_2 adsorption capacity because of the highest oxygen vacancies and basicity while 10 wt% Ni–$Ce_{0.003}Ti_{0.997}O_2$ catalyst had the highest H_2 adsorption capacity on the surface. However, the highest CO_2 methanation catalytic activity was found when 10 wt% Ni–$Ce_{0.003}Ti_{0.997}O_2$ was used as a catalyst. It can be explained that the CO_2 methanation reaction on the prepared catalysts depended on the amount of H_2 that was adsorbed and dissociated to form H atoms on the catalyst surface. Moreover, an excess of adsorbed amounts of CO_2 on the surface can suppress and inhibit the adsorption of H_2 on the catalyst surface. Therefore, it can be said that adsorbed H atoms on the catalyst surface was the limiting reagent and the main factor that improved the CO_2 methanation catalytic activity of the prepared catalyst in this work.

4. Conclusion

10 wt% Ni–$Ce_xTi_{1-x}O_2$ ($x = 0$, 0.003, 0.05, 0.10 and 0.15) catalysts were prepared and characterized by several techniques. The catalytic activity of the prepared catalysts was studied for the CO_2 methanation reaction. The 10 wt% Ni–$Ce_{0.003}Ti_{0.997}O_2$ catalyst displayed the best CO_2 methanation catalytic activity which showed the highest CO_2 conversion and CH_4 yield with low CO yield entire the reaction temperature range. The role of Ce addition on TiO_2-supported Ni in enhancing CO_2 methanation catalytic activities were discussed in term of surface, structural, electrical and redox properties changes. The electronic state of Ni species during pretreatment and CO_2 methanation showed that the active state of Ni species was Ni^0 which can be activated by being pretreated under H_2 flowing at 450 °C and this active state remained unchanged during the reaction. The role of Ce in enhancing the CO_2 methanation catalytic activity of TiO_2-supported Ni was to modify the catalyst properties as follows;

(i) Ce can promote the dispersion of Ni on catalysts surface and also prevent the sintering of Ni species during the reaction which can lead to high catalytic activity and high stability.

(ii) Upon the incorporation of Ni into TiO_2 lattice, the expansion of unit cell and oxygen vacancies were observed and further increased of Ce loading led to higher degree of unit cell enlargement and larger amount of oxygen vacancies formation. Moreover, Ce can increase the basicity of catalysts, which can be evidenced by CO_2 adsorption results. It can be seen that higher amounts of Ce led to high CO_2 adsorption. However, excess amounts of CO_2 adsorption can also inhibit the H_2 adsorption on the catalyst surface leading to lowering of catalytic activities.

(iii) Ce can increase the reducibility of the catalyst by facilitating reduction of Ni^{2+} to Ni^0 at lower temperature.

Therefore, it can be explained that the CO_2 methanation reaction on the prepared catalysts depends on the adsorbed H_2 amount on the catalyst surface, or that the adsorbed H_2 on the catalyst surface was the limiting reagent and the main factor

that improved the CO_2 methanation catalytic activity of the prepared catalyst. Furthermore, the catalytic stability of the 10 wt% Ni–$Ce_{0.003}Ti_{0.997}O_2$ catalyst was investigated at 350 °C for 50 h. The result exhibited that the 10 wt% Ni–$Ce_{0.003}Ti_{0.997}O_2$ catalyst was greatly stable CO_2 conversion, CH_4 yield and CH_4 selectivity entire 50 h of stability test.

Conflicts of interest

There are no conflicts of interest to declare

Acknowledgements

References

1 I. Dimitriou, P. Garcıa-Gutierrez, R. H. Elder, R. M. Cuéllar-Franca, A. Azapagicb and R. W. K. Allena, *Energy Environ. Sci.*, 2018, **8**, 1775–1789.

2 M. A. A. Aziz, A. A. Jalil, S. Triwahyono and A. Ahmad, *Green Chem.*, 2015, **17**, 2647–2663.

3 J. Park and E. W. McFarland, *J. Catal.*, 2009, **266**, 92–97.

4 J. Gao, Y. Wang, Y. Ping, D. Hu, G. Xu, F. Gu and F. Su, *RSC Adv.*, 2012, **2**, 2358–2368.

5 J. Gao, Q. Liu, F. Gu, B. Liu, Z. Zhong and F. Su, *RSC Adv.*, 2015, **5**, 22759–22776.

6 J. R. Rostrup-Nielsen, K. Pedersen and J. Sehested, *Appl. Catal.*, 2007, **330**, 134–138.

7 T. T. M. Nguyen, L. Wissing and M. S. Skjøth-Rasmussen, *Catal. Today*, 2013, **215**, 233–238.

8 W. Wang, S. Wang, X. Ma and J. Gong, *Chem. Soc. Rev.*, 2011, **40**, 3703–3727.

9 I. Fechete and J. C. Vedrine, *Molecules*, 2015, **20**, 5638–5666.

10 P. Riani, G. Garbarinob, M. A. Lucchini, F. Canepa and G. Busca, *J. Mol. Catal. A: Chem.*, 2014, **383–384**, 10–16.

11 D. Pandey, K. Ray, R. Bhardwaj, S. Bojja, K. V. R. Chary and G. Deo, *Int. J. Hydrogen Energy*, 2018, **43**, 4987–5000.

12 J. Lin, C. Ma, Q. Wang, Y. Xu, G. Ma and J. Wang, *Appl. Catal., B*, 2019, **243**, 262–272.

13 R. Ye, W. Gong, Z. Sun, Q. Sheng, X. Shi, T. Wang, Y. Yao, J. J. Razink, L. Lin, Z. Zhou, H. Adidharma, J. Tang, M. Fan and Y. Yao, *Energy*, 2019, **188**, 116059.

14 M. Wolf, L. Hui Wong, C. Schüler and O. Hinrichsen, *J. CO2 Util.*, 2020, **36**, 276–287.

15 J. Guilera, J. d. Valle, A. Alarcón, J. A. Díaz and T. Andreu, *J. CO2 Util.*, 2019, **30**, 11–17.

16 S. Tada, S. Ikeda, N. Shimoda, T. Honma, M. Takahashi, A. Nariyuki and S. Satokawa, *Int. J. Hydrogen Energy*, 2017, **42**, 30126–30134.

17 B. Lu and K. Kawamoto, *Catal. Sci. Technol.*, 2014, **4**, 4313–4321.

18 M. A. A. Aziz, A. A. Jalil, S. Triwahyono, R. R. Muktid, Y. H. Taufiq-Yap and M. R. Sazegar, *Appl. Catal., B*, 2014, **147**, 359–368.

19 S. Rönsch, J. Schneider, S. Matthischke, M. Schlüter, M. Götz, J. Lefebvre, P. Prabhakaran and S. Bajohr, *Fuel*, 2016, **166**, 276–296.

20 Q. Pan, J. Peng, T. Sun, S. Wang and S. Wang, *Catal. Commun.*, 2014, **45**, 74–78.

21 T. A. Le, M. S. Ki, S. H. Lee, T. W. Kim and E. D. Park, *Catal. Today*, 2017, **293–294**, 89–96.

22 M. Yamasaki, M. Komori, E. Akiyama, H. Habazaki, A. Kawashima, K. Asami and K. Hashimoto, *Mater. Sci. Eng.*, 1999, **A267**, 220–226.

23 H. Takano, K. Izumiya, N. Kumagai and K. Hashimoto, *Appl. Surf. Sci.*, 2011, **257**, 8171–8176.

24 Ni. Perkas, G. Amirian, Z. Zhong, J. Teo, Y. Gofer and A. Gedanken, *Catal. Lett.*, 2009, **130**, 455–462.

25 G. Zhi, X. Guo, Y. Wang, G. Jin and X. Guo, *Catal. Commun.*, 2011, **16**, 56–59.

26 H. Liu, X. Zou, X. Wang, X. Lu and W. Ding, *J. Nat. Gas Chem.*, 2012, **21**, 703–707.

27 C. Gaudillere, L. Navarrete and J. M. Serra, *Int. J. Hydrogen Energy*, 2017, **42**, 895–905.

28 W. Li, H. Wang, X. Jiang, J. Zhu, Z. Liu, X. Guo and C. Song, *RSC Adv.*, 2018, **8**, 7651–7669.

29 P. Frontera, A. Macario, M. Ferraro and P. Antonucci, *Catalysts*, 2017, **7**, 59.

30 L. Bian, L. Zhang, R. Xia and Z. Li, *J. Nat. Gas Sci. Eng.*, 2015, **27**, 1189–1194.

31 S. Tada, O. J. Ochieng, R. Kikuchi, T. Haneda and H. Kameyama, *Int. J. Hydrogen Energy*, 2014, **39**, 10090–10100.

32 P. Kidkhunthod, *Adv. Nat. Sci.: Nanosci. Nanotechnol.*, 2017, **8**, 035007.

33 W. Klysubun, P. Kidkhunthod, P. Tarawarakarn, P. Sombunchoo, C. Kongmark, S. Limpijumnong, S. Rujirawat, R. Yimnirun, G. Tumcharern and K. Faungnawakij, *J. Synchrotron Radiat.*, 2017, **24**, 707–716.

34 C. M. Kalamaras, S. Americanou and A. M. Efstathiou, *J. Catal.*, 2011, **279**, 287–300.

35 N. Li, X. Zou, M. Liu, L. Wei, Q. Shen, R. Bibi, C. Xu, Q. Ma and J. Zhou, *J. Phys. Chem. C*, 2017, **121**, 25795–25804.

36 Y. Jiang, Z. Jin, C. Chen, W. Duan, B. Liu and X. Chen, *RSC Adv.*, 2017, **7**, 12856–12870.

37 M. Tahir and N. A. S. Amin, *Appl. Catal., B*, 2015, **162**, 98–109.

38 S. Rajendran, D. Manojb, K. Raju, D. D. Dionysioud, M. Naushade, F. Graciaf, L. Cornejo, M. A. Gracia-Pinillag and T. Ahamad, *Sens. Actuators, B*, 2018, **264**, 27–37.

39 D. A. H. Hanaor and C. C. Sorrell, *J. Mater. Sci.*, 2011, **46**, 855–874.

40 D. R. Shinde, P. S. Tambade, M. G. Chaskar and K. M. Gadave, *Drinking Water Eng. Sci.*, 2017, **10**, 109–117.

41 H. Yan, D. Zhang, J. Xu, Y. Lu, Y. Liu, K. Qiu, Y. Zhang and Y. Luo, *Nanoscale Res. Lett.*, 2014, **9**, 1–7.

42 L. Li, F. Chen, J. Q. Lu and M. F. Luo, *J. Phys. Chem. A*, 2011, **115**, 7972–7977.

43 S. L. Reis, E. C. C. Souza and E. N. S. Muccillo, *Solid State Ionics*, 2011, **192**, 172–175.

44 B. Choudhury, B. Borah and A. Choudhury, *Photochem. Photobiol.*, 2012, **88**, 257–264.

45 S. Esposito, *Materials*, 2019, **12**, 668.

46 V. R. Akshay, B. Arun, G. Mandal and M. Vasundhar, *Phys. Chem. Chem. Phys.*, 2019, **21**, 2519–2532.

47 F. Ocampo, B. Louis and A. Roger, *Appl. Catal., A*, 2009, **369**, 90–96.

48 K. C. Chanapattharapol, S. Krachuamram, A. Makdee, P. Unwiset and S. Srikwanjai, *J. Rare Earths*, 2017, **35**, 1197–1205.

49 Z. Fan, F. Meng, J. Gong, H. Li, Z. Ding and B. Ding, *J. Mater. Sci.: Mater. Electron.*, 2016, **27**, 11866–11872.

50 L. Xu, F. Wang, M. Chen, D. Nie, X. Lian, Z. Lu, H. Chen, K. Zhang and P. Ge, *Int. J. Hydrogen Energy*, 2017, **42**, 15523–15539.

51 E. R. Aluri and A. P. Grosvenor, *Phys. Chem. Chem. Phys.*, 2013, **15**, 10477–10486.

52 F. de Groot, *Chem. Rev.*, 2001, **101**, 1779–1808.

53 C. Wattanawikkam, W. Pecharapa and K. N. Ishihara, *Ceram. Int.*, 2017, **43**, S397–S402.

54 M. Sahoo, A. K. Yadav, S. N. Jha, D. Bhattacharyya, T. Mathews, N. K. Sahoo, S. Dash and A. K. Tyagi, *J. Phys. Chem. C*, 2015, **119**, 17640–17647.

55 B. Hsieh, M. Tsai, C. Pan, W. Su, J. Rick, J. Lee, Y. Yang and B. Hwang, *NPG Asia Mater.*, 2017, **9**, e403.

56 K. Huang, K. Sasaki, R. R. Adzic and Y. Xing, *J. Mater. Chem.*, 2012, **22**, 16824–16832.

57 T. Tangcharoen, W. Klysubun and C. Kongmark, *J. Mol. Struct.*, 2018, **1156**, 524–533.

58 J. K. Kesavan, I. Luisetto, S. Tuti, C. Meneghini, G. Iucci, C. Battocchio, S. Mobilio, S. Casciardi and R. Sisto, *J. CO2 Util.*, 2018, **23**, 200–211.

59 T. Tangcharoen, W. Klysubun and C. Kongmark, *J. Mol. Struct.*, 2019, **1182**, 219–229.

60 X. Meng, C. Wan, Y. Wang and X. Ju, *J. Alloys Compd.*, 2018, **735**, 1637–1647.

61 A. Worayingyong, S. Sang-urai, M. F. Smith, S. Maensiri and S. Seraphin, *Appl. Phys. A: Mater. Sci. Process.*, 2014, **117**, 1191–1201.

62 K. C. Chanapattharapol, S. Krachuamram, P. Kidkhunthod and Y. Pooarporn, *Solid State Sci.*, 2020, **99**, 106066.

63 P. Helden, J. Berga and I. M. Ciobîcă, *Catal. Sci. Technol.*, 2012, **2**, 491–494.

64 J. Liu, C. Li, F. Wang, S. He, H. Chen, Y. Zhao, M. Wei, D. G. Evans and X. Duan, *Catal. Sci. Technol.*, 2013, **3**, 2627–2633.

65 M. A. A. Aziz, A. A. Jalil, S. Triwahyono and S. M. Sidik, *Appl. Catal., A*, 2014, **486**, 115–122.

66 L. Xu, F. Wang, M. Chen, J. Zhang, K. Yuan, L. Wang, K. Wu, G. Xu and W. Chen, *RSC Adv.*, 2016, **6**, 28489–28499.

67 B. Bharti, S. Kumar, H. Lee and R. Kumar, *Sci. Rep.*, 2016, **6**, 32355.

68 F. Wang, S. He, H. Chen, B. Wang, L. Zheng, M. Wei, D. G. Evans and X. Duan, *J. Am. Chem. Soc.*, 2016, **138**, 6298–6305.

69 A. Quindimil, U. De-La-Torre, B. Pereda-Ayo, J. A. González-Marcos and J. R. González-Velasco, *Appl. Catal., B*, 2018, **238**, 393–403.

70 H. Y. Kim, H. M. Lee and J. Park, *J. Phys. Chem. C*, 2010, **114**, 7128–7131.

71 M. Ding, J. Tu, Q. Zhang, M. Wang, N. Tsubaki, T. Wang and L. Ma, *Biomass Bioenergy*, 2016, **85**, 12–17.

72 F. B. Noronha, E. C. Fendley, R. R. Soares, W. E. Alvarez and D. E. Resasco, *Chem. Eng. J.*, 2001, **82**, 21–31.

73 J. Ren, H. Guo, J. Yang, Z. Qin, J. Lin and Z. Li, *Appl. Surf. Sci.*, 2015, **351**, 504–516.